QUASI-STATIC MODEL OF MAGNETICALLY COLLIMATED JETS AND RADIO LOBES. II. JET STRUCTURE AND STABILITY

Stirling A. Colgate[1], T. Kenneth Fowler[2], Hui Li[1], E. Bickford Hooper[3,4], Joseph McClenaghan[5], and Zhihong Lin[5]

[1] Theoretical Division, Los Alamos National Laboratory, Los Alamos, NM 87545, USA
[2] University of California, Berkeley, CA 94720, USA
[3] Lawrence Livermore National Laboratory, Livermore, CA 94550, USA
[4] Present Address: Woodruff Scientific, Seattle, WA 98103, USA
[5] University of California, Irvine, CA 92697, USA

ABSTRACT

This is the second in a series of companion papers showing that when an efficient dynamo can be maintained by accretion disks around supermassive black holes in active galactic nuclei, it can lead to the formation of a powerful, magnetically driven, and mediated helix that could explain both the observed radio jet/lobe structures and ultimately the enormous power inferred from the observed ultrahigh-energy cosmic rays. In the first paper, we showed self-consistently that minimizing viscous dissipation in the disk naturally leads to jets of maximum power with boundary conditions known to yield jets as a low-density, magnetically collimated tower, consistent with observational constraints of wire-like currents at distances far from the black hole. In this paper we show that these magnetic towers remain collimated as they grow in length at nonrelativistic velocities. Differences with relativistic jet models are explained by three-dimensional magnetic structures derived from a detailed examination of stability properties of the tower model, including a broad diffuse pinch with current profiles predicted by a detailed jet solution outside the collimated central column treated as an electric circuit. We justify our model in part by the derived jet dimensions in reasonable agreement with observations. Using these jet properties, we also discuss the implications for relativistic particle acceleration in nonrelativistically moving jets. The appendices justify the low jet densities yielding our results and speculate how to reconcile our nonrelativistic treatment with general relativistic MHD simulations.

Key words: accretion, accretion disks – galaxies: active – galaxies: jets – magnetic fields – magnetohydrodynamics (MHD) – stars: black holes

1. INTRODUCTION

This is the second in a series of papers building on Colgate & Li ([2004](#)), in which it was hypothesized that ultrahigh-energy cosmic rays $\sim 10^{20}$ eV (UHECRs) are created by an accelerating ion current in powerful radio jet/lobes created by active galactic nuclei (AGNs). In our first paper (Colgate et al. [2014](#), hereafter Paper I), we derived the magnetic fields generated by an accretion disk dynamo, by analogy with a Faraday disk. Here we show that jet ejection and propagation are analogous to low-density jets created in the laboratory (e.g., Zhai et al. [2014](#)). As in our treatment of accretion disks in Paper I, we will not attempt to explain jets in detail, but instead we hope to identify simple models capturing the key physics.

AGN jets are created when the accretion power stretches field lines high above the disk. In our model, the disk ends and the jet begins in a coronal region of the disk where density and pressure due to accretion fall to a very low value (Bisnovatyi-Kogan & Lovelace [2012](#)). This line of reasoning has led us to an essentially one-dimensional model of magnetic jets with negligible density and pressure, similar to the so-called magnetic tower model, as proposed by Lynden-Bell ([1996](#)) and studied further in a series of papers (e.g., Li et al. [2001](#); Lynden-Bell [2003](#), [2006](#); Uzdensky & MacFadyen [2006](#)) and numerically (e.g., Lovelace et al. [2002](#); Kato et al. [2004](#); Li et al. [2006](#); Nakamura et al. [2006](#), [2007](#), [2008](#)).

We have in mind the configuration of Figure 1, shown also in Paper I, repeated here for convenience. This is a cross section of magnetic flux surfaces leaving the disk and returning at the "nose" at the top of the figure. Currents follow field lines above the disk but cross the fields inside the disk to form closed loops, as they would in a Faraday disk. In Figure 1, outgoing jet power is concentrated in a central column, surrounded by an extensive diffuse pinch with lower current density.

It is this theoretical separation of the jet/disk system into a compact central column surrounded by a broad diffuse pinch that is the main source of simplification in our model, made concrete by defining the diffuse pinch zone as the region where disk rotation is approximately Keplerian. In Paper I, we showed that a Keplerian diffuse pinch necessarily terminates at a radius $r = a$ that turned out to be about 10 Schwarzschild radii, so the dynamics is nonrelativistic in the diffuse pinch zone of the disk as well as in the magnetic helix/jet it creates above the disk. As a further simplification, we represented the relativistic central column as an electric circuit, as in early models of quasars (e.g., Chapter 9 of Frank et al. [2002](#); Lovelace & Kronberg [2013](#)). Furthermore, coupling this diffuse pinch model to the central column electric circuit turned out to determine the amount of current I passing through the central column, as discussed below.

To set the stage for presenting our magnetic helix/jet model, in the remainder of this Introduction, we review the results in Paper I in order to explain how our model of accretion disks in Paper I provides boundary conditions that fix magnetic tower solutions. Towers are described by the force-free condition, $c^{-1} \boldsymbol{j} \times \boldsymbol{B} + \sigma \boldsymbol{E} = 0$, with charge density σ (Frank et al. [2002](#)). Then the equation to be solved in the long straight section of the jet is (in cylindrical coordinates $\{r, \phi, z\}$ with height z
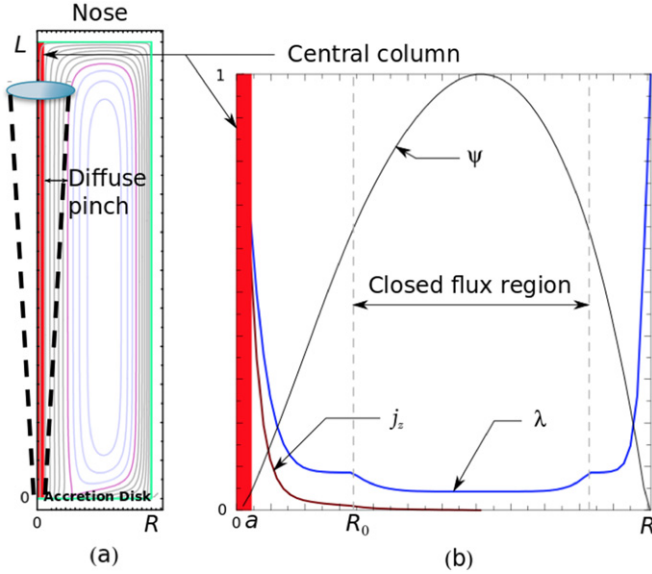
Figure 1. Left: a simplified sketch of an accretion disk ejecting a jet, overlaid by a GS solution for the cross section of poloidal (B_z, B_r) magnetic flux surfaces, using the accretion disk boundary condition derived in the Introduction. The axisymmetric calculation box is a cylinder of radius R and height L. The jet current is concentrated in a central column of radius a calculated in the text, surrounded by a diffuse pinch of radius R_0 and an extended outer region of radius R bounded by the return current. Note that outgoing flux surfaces are straight, finally turning at the "nose." Right: also drawn are the poloidal flux function Ψ, the poloidal current j_z, and the function $\lambda = |j_z/B_z|$ depicted at $z = L/2$ midway up the column. The figure is a 2D average, the dotted cone depicting the apparent shape of jets due to 3D effects discussed in Section 5.

above the disk)

$$\frac{\partial B_z^2}{\partial r} + \frac{1}{r^2}\frac{\partial\left[r^2\left(B_\phi^2 - E_r^2\right)\right]}{\partial r} = 0; \quad \text{at } r > a, \; |z| > H. \quad (1)$$

While in Appendix C we will see that $E_r = B_\phi$ can kill the magnetic "pinch" force in relativistic jets, here we consider only the low-density, nonrelativistic diffuse pinch region at $r > a$ where pressure is negligible and E_r is small. Then the pinch force maintains collimation, allowing us also to set $B_r = 0$, giving a one-dimensional (1D) model of the jet valid except near the "nose" at the top of Figure 1 or near the disk, though in fact we find below that $B_r = 0$ in the corona.

Even with $E_r = B_r = 0$, Equation (1) has two unknowns, B_z and B_ϕ. The main result in Paper I is a boundary condition fixing the solution, one very different from the "freezing in" of flux in the disk as assumed by Lynden-Bell (1996, 2003), Li et al. (2001), and many other authors (see, e.g., Frank et al. 2002). Our boundary condition comes from coupling of the disk interior to its corona via the conservation of angular momentum, given in Paper I (see Equation (5) in that paper), written here as

$$\{\text{K.E.}\} + \frac{1}{r}\frac{\partial\left(r\rho v_r r^2\Omega\left[1 - (\nu/v_r)\partial(\ln\Omega)/\partial r\right]\right)}{\partial r}$$
$$= \frac{1}{4\pi}\frac{\partial\left(rB_\phi B_z\right)}{\partial z} + \left\{\frac{1}{4\pi r}\frac{\partial\left(r^2 B_r B_\phi\right)}{\partial r}\right\}, \quad (2a)$$

$$\frac{1}{r}\frac{\partial\left(r\rho v_r r^2\Omega_K g\right)}{\partial r} = \frac{1}{4\pi}\frac{\partial\left(rB_\phi B_z\right)}{\partial z}, \quad (2b)$$

with accretion velocity v_r, disk density ρ, Keperian rotation frequency Ω_K, and K.E. representing other terms from the stress tensor and so on. In going from Equations (2a–b), we have dropped all the terms in $\{...\}$ and absorbed the effects of disk viscosity ν into the term g. Furthermore, we can take the limit $g \approx 1$, using an ordering scheme in the diffuse pinch zone, given by

$$\left|rB_r/(HB_z)\right| \approx \left|v_r/r\Omega_K\right| \ll 1, \quad (3)$$

$$g \approx 1 - \left|\nu/(rv_r)\right| \approx 1 - \left|v_r/(r\Omega_K)\right|^{1/2}(a/r), \quad (4)$$

where H is the scale height of the corona above the disk midplane. Here $|rB_r/(HB_z)|$ is the ratio of the term in $\{...\}$ on the right-hand side (rhs) of Equation (2a) to the magnetic term retained. That this ratio is small justifies dropping B_r in Equation (1) even at the corona, and this also eliminates the centrifugal ejection of mass proposed in Blandford & Payne (1982) (see discussion in Section 3.1). All approximations giving Equations (3) and (4) are verified term by term in Paper I, using the hyperresistive Ohm's Law introduced in Equation (10) below in order to calculate various ratios of $\boldsymbol{\nu}$ and $\boldsymbol{B}$ in comparing terms in the angular momentum equation.

Using Equation (2b), setting $g = 1$ and integrating $0 < z < H$, we obtain (Lovelace et al. 2009)

$$\dot{M}\Omega_K\big/2 = \left(rB_\phi\left|B_z\right|\right)_{r,H} \quad \text{for } r > a, \quad (5)$$

where $\dot{M} = dM/dt \approx 4\pi r\rho\left|v_r\right|H$ is the accretion rate with black hole mass M, and $\Omega_K^2 = GM/r^3$ is the Keplerian rotation with Newtonian gravitational constant G. In Paper I, we found an exact simultaneous solution to Equations (1) and (5) that is well-approximated by first setting rB_ϕ constant in Equation (5) to find B_z, then substituting this B_z into Equation (1) to find corrections to B_ϕ. We obtain

$$B_\phi(r) \approx B_a[aI(r)/(rI)]; \quad \left|B_z(r)\right| \approx B_a(a/r)^{3/2};$$
$$B_r \approx 0, \quad \text{for } r \geqslant a, \quad (6)$$

$$I(r) = \int_0^r 2\pi r dr j_z \approx 1.7I[1 - 0.6(a/r)]^{1/2}, \quad (7)$$

where the magnitude B_a (same for B_ϕ and B_z) is derived in Section 6, and the coefficients in Equation (7) are chosen to agree with the exact results at $r = a$ and $r \to \infty$. The quantity I is the total current inside the central column (within radius a), and $I(r)$ includes the current from both the central column and the diffuse pinch (up to r). The fraction of the circulating current passing through the central column is determined to be equal to $1/1.7 \sim 60\%$.

Equation (6) will serve as the boundary condition for our jet solution in Section 3, extrapolated beyond $r = R_0$ where $B_z = 0$, as discussed in Section 3.1. Physically, this boundary condition is the unique consequence of electromagnetic ejection of angular momentum on the rhs of Equation (5), to be compared with the Poynting energy flux found by multiplying the rhs of Equation (5) by Ω_K. How to get rid of angular momentum is the classic problem of accretion theory (Frank et al. 2002), first solved by postulating a large hydrodynamic viscosity ν that recycles most of the angular momentum in the classic accretion model of Shakura & Sunyaev (1973). In Appendix A of Paper I, we found that taking $|v_r/r\Omega_K|$ to be

small as in Equation (3) is consistent with a viscosity factor $|\nu/rv_r| \ll 1$ in the diffuse pinch zone of the accretion disk, giving $g \approx 1$ in Equation (4), giving then the maximum transfer of accretion power to Poynting power. Additional evidence showing consistency with $|v_r/r\Omega_K| \ll 1$ in the diffuse pinch is given in Section 6. A previous study on accretion and outflow from dissipationless disks is given in Bogovalov & Kelner (2010) as well.

The remainder of the paper is organized as follows. In Section 2 we justify using our unconventional nonrelativistic magnetic tower model to describe the magnetic structures of AGN jets. In Section 3 we first show why our straight 1D tower model approximates two-dimensional (2D) jets, then use our model to calculate the expansion velocity of the magnetic helix/jet. In Sections 4 and 5 we examine jet stability to show why unstable jets remain collimated, yet provide the power illuminating the giant radio lobes by synchrotron radiation. In Section 6 we calculate jet dimensions. In Section 7 we compare predictions with observations and experiments. In Section 8 we summarize results and compare our model with other models. Appendix A justifies our quasi-static model of jet propagation. Appendix B pins down the voltage in our circuit model. Finally, Appendix C attempts to reconcile our model with general relativistic MHD simulations.

Throughout the paper we will continue to use a cylindrical coordinate system $\{r, \phi, z\}$ in which the disk spins about a fixed z axis with an angular frequency Ω pointing along the $+\hat{z}$ direction in the inner region of the disk, giving positive B_ϕ and negative B_z in the same region. Units are in cgs, often introducing c, the speed of light.

2. CAN A MAGNETIC TOWER MODEL EXPLAIN AGN JETS?

As discussed in the Introduction, our jet is a magnetic tower model in which magnetic forces collimate the jet, as in Figure 1. A principal feature of this model is its central column with constant radius a. We acknowledge that our claim that the axisymmetrically averaged current channel maintains a constant radius, as it would if only magnetic forces are present, is contrary to many previous jet models, including relativistic models in which the electric force spoils magnetic collimation when the flow speed approaches the speed of light. Motivated by the observed superluminal motions of features within AGN jets (e.g., Wardle et al. 1994; Zensus et al. 1995; Lister et al. 2013; Homan et al. 2015), it is generally thought that AGN jets (as bulk plasmas) can be quite relativistic if the superluminal features are interpreted as real plasma motion. One primary goal of many previous 2D axisymmetric relativistic MHD studies has focused on how to start the jets in a Poynting-flux-dominated regime and gradually convert the jet into a kinetic-energy-dominated regime, while at the same time achieving both collimation and jet acceleration (e.g., Chiueh et al. 1991; Li et al. 1992; Appl & Camenzind 1993; Eichler 1993; Bogovalov 1995; Vlahakis & Königl 2003; Beskin & Nokhrina 2006; Komissarov et al. 2007, 2009; Narayan et al. 2007; Tchekhovskoy et al. 2008; Lyubarsky 2009; Beskin 2010). One important question that is still under intense study is the stability of such jet structures, especially the role of current-driven kink instabilities (e.g., Appl & Camenzind 1992; Istomin & Pariev 1996; Lyubarsky 1999; Mizuno et al. 2007; McKinney & Blandford 2009; Narayan et al. 2009; ONeill et al. 2012; Bromberg & Tchekhovskoy 2015; Porth &

Komissarov 2015). In these studies, detailed knowledge of the poloidal flux B_z is often needed in order to examine the jet stability, although the origin and distribution of B_z are not well constrained. Recent reviews on jet instabilities can be found in Hardee (2011) and Perucho (2012).

While these relativistic MHD studies have certainly improved our understanding of jets, many important questions remain. A critical assumption in many models is the existence of a large-scale global poloidal magnetic flux that is often assumed to be nonzero (i.e., having a net flux in the domain of interest) and threading through the disk and the black hole. By contrast, tower models like ours start with zero net global magnetic flux, as proposed by Lynden-Bell (1996) and studied further in a series of papers as cited earlier. Recently, the dynamic evolution of a magnetic tower jet in the three-dimensional (3D) relativistic limit is studied in Guan et al. (2014), where it was shown that such jets can continue propagating without suffering catastrophic destruction even though the current-driven kink instabilities (and possibly Kelvin–Helmholtz instability) are quite visible.

In the context of the magnetic tower model, we have proposed an alternative view of AGN jets as described in Paper I. This model presents several key features that are significantly different from the more traditional views: (1) the large-scale poloidal flux threading the disk is produced by an accretion disk dynamo with closed flux surfaces, as in Figure 1; (2) the existence of this dynamo-sustained field leads to the removal of disk angular momentum and establishment of a cylindrical, helical magnetic structure; (3) the plasma mass density and kinetic energy density are much less than the magnetic energy density inside this structure; (4) this structure maintains quasi-magnetic equilibrium as the overall structure expands axially and radially at a rate that is nonrelativistic, in part due to inductance and in part due to shocks in the ambient, as explained in Section 3.3; (5) the instability of the jet is already determined by the diffuse pinch at $r > 10R_s$, where the dynamics is nonrelativistic; and (6) as in early models of quasars (Frank et al. 2002), the central column inside the diffuse pinch can be represented by an electric circuit with current and voltage determined by the diffuse pinch zone of the accretion disk.

Here we suggest further that the observed superluminal motions are not necessarily due to bulk plasma motion, but instead they could be "features" or "perturbations" that propagate superluminally. In fact, observations by the Monitoring Of Jets in Active galactic nuclei with VBLA Experiments (MOJAVE) project have deduced that, though rare, a small percentage of sources showed inward apparent motion (Lister et al. 2009). Furthermore, detailed studies of 15 and 43 GHz observations of M87 have revealed large discrepancies in observed proper motions (e.g., Komissarov et al. 2007; Walker et al. 2008; Nakamura & Asada 2013; Asada et al. 2014). So, we believe that the remaining uncertainties in directly relating the observed superluminal features with bulk plasma motion leave room for alternative interpretations. For our tower model alternative, we argue that the central column of the magnetic structure will undergo 3D MHD instabilities that produce wandering field lines that cause some amount of dissipation along the central axis, leading to the appearance of a cone with an opening angle as well as superluminal features (see Figure 1 and discussions in Section 5.2). Nonetheless, the majority of the jet energy is

still stored in a quasi-2D axisymmetric component of the magnetic fields.

Several previous studies in the literature support our claim that AGN jets can be magnetically collimated. We note especially Faraday rotation measurements and other magnetic signatures far from black holes that can be interpreted as arising from the thin wire-like current filaments of our model (e.g., Owen et al. 1989; Kronberg et al. 2011; Lovelace & Kronberg 2013). Second, we note evidence that radio lobes themselves are confined by large current loops pushing against the ambient (Diehl et al. 2008, discussed in Section 7). Third, we note that in Section 3.3 we can show how the large magnetic inductance of our wire-like structure slows down the jet propagation velocity, yielding $dL/dt \approx 0.01c$, which provides a straightforward explanation of the longest observed AGN jets. Fourth, in Section 5 we will explain how our jets collimated in 2D can produce field lines wandering in 3D that might account for the apparent shape of jets as determined from synchrotron and other radiations. Fifth, in Appendix A we justify the low jet densities, allowing us to neglect kinetic effects in jets, these low densities arising from the disk model of Paper I, which leads us to conclude that the most likely mechanism ejecting ions against black hole gravity is an electrostatic sheath (Lovelace 1976). Finally, as an ongoing issue, in Appendices B and C we suggest that including the effects of ion acceleration and shocks in the low intergalactic density would slow down jets so that relativistic jets in idealized simulations would become the nonrelativistic jets of our model (Guan et al. 2014). With these justifications, in this paper we simply ask what would be the consequences if jets do behave like our nonrelativistic magnetically collimated model, thus allowing us to draw on extensive knowledge from similar jets in the laboratory.

3. JET PROPAGATION

We begin our discussion of how jets propagate by first verifying that the straight 1D jet model described in the Introduction is a good approximation to the actual 2D structure in Figure 1. We do this using the MHD momentum equations in the Grad–Shafranov (GS) form for the case of negligible plasma density and pressure, as argued in Appendix A.
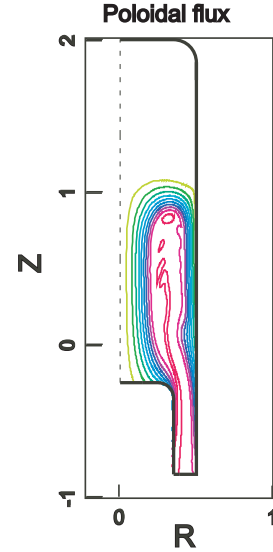
3.1. Grad–Shafranov Solution

The 2D version of Equation (1) is the well-known GS equation (e.g., Shafranov 1957; Grad 1960), much employed in astrophysics (e.g., Li et al. 2001; Beskin 2010), and in relativistic form (e.g., Michel 1969; Okamoto 1974). The GS equation is derived from the mean-field momentum equation by expressing $\boldsymbol{B} = \nabla \times \boldsymbol{A}$ in terms of the poloidal flux $\Psi = rA_\phi$ and factoring out $\nabla\Psi$ to obtain

$$\left\{ \frac{1}{v_A^2}\frac{\partial^2\Psi}{\partial t^2} + r^2(4\pi\sigma)\frac{\partial\Phi}{\partial\Psi} \right\} + \Delta^*\Psi + I_p\frac{\partial I_p}{\partial\Psi} = 0$$

$$\Delta^*\Psi = \left[r\frac{\partial}{\partial r}\big(r^{-1}\partial\Psi/\partial r\big) + \frac{\partial^2\Psi}{\partial z^2} \right], \qquad (8)$$

where $I_p = rB_\phi$ and Φ is the electrostatic potential giving E_r in Equation (1). We have added an unconventional time-dependent term as an approximation to $\rho\,\partial(\gamma_L\boldsymbol{v})/\partial t$ with $E_\phi \approx -(1/cr)\partial\Psi/\partial t$, giving $\boldsymbol{v} = -c(\boldsymbol{E}_\phi \times \boldsymbol{B}/B^2) = r^{-1}[(\partial\Psi/\partial t)\hat{\phi} \times \boldsymbol{B}/B^2] = r^{-2}(\partial\Psi/\partial t)\nabla\Psi/B^2$ with $\nabla\Psi$

Figure 2. Poloidal flux during helicity injection in the laboratory, from a resistive MHD simulation (Hooper et al. 2012). All units are in meters. The geometry is very similar to the SSPX experiment except that the height of the electrically conducting flux conserver (heavy lines) has been increased to 2. The coaxial gun located at $Z = -0.8$ injects toroidal flux. The current generating that flux pinches around the geometric axis (dotted line at $R = 0$), with the return current at the flux-conserver radius at $R = 0.5$. The initial poloidal flux lines are generated by magnetic coils inside the gun at $R < 0.3$, and these flux lines have been stretched upward. At the time of this "snapshot," the injected flux has not yet expanded sufficiently to fill the flux conserver, but it shows both the collimation along Z and the "blunt nose" feature at $Z \sim 1$.

factored out as in the equilibrium GS derivation; keeping the Lorentz factor $\gamma_L \approx [1 - (v/c)^2]^{-1/2}$ reminds us that v_A is relativistic in jets produced by accretion disks. We have also omitted kinetic forces in jets that play an important role in defining Mach numbers in some jet models (Beskin 2010), while in Paper I, reviewed in the Introduction, we found that disk rotation and accretion are the only kinetic effects of importance.

Jet propagation is a competition between the jet propagation at Alfvén velocities, approximated by Equation (8), and the available power. In Section 3.3, we show why propagation of an AGN jet of growing length L is always power limited, yielding $dL/dt \ll v_A$. In Appendices B and C, we show that the electric field becomes small compared to the magnetic field except very near the black hole. This allows us to drop $\partial\Phi/\partial\Psi$ in Equation (8). Also we use $v_A \gg r(\partial/\partial t)$ to justify dropping $(1/v_A^2)\partial^2\Psi/\partial t^2$ in order to calculate the magnetic field as a succession of equilibria inside a prescribed volume if that volume were known.

That the volume can be approximated as a cylinder with slowly increasing length L also follows for the large value of $v_A \approx c$ in jets, as shown in Appendix A. The large Alfvén velocity compared to dL/dt gives plenty of time for magnetic forces to flatten the nose in the radial direction as the length changes slowly in the z direction. This is clearly seen in the blunt-nosed shape of the plasma in Figure 2, showing an MHD simulation of spheromak formation (see also Section 3.2). It is this argument for a persistent blunt-nosed shape that allows us to calculate jets as equilibria inside the cylindrical shape in Figure 1. We approximate the radius R of radio lobes as a constant, noting that R will turn out to appear only logarithmically in our model, so a simple right-circular cylinder

suffices, even for jets distorted in shape by external forces but gently compared to the tiny radius of the central column (see, e.g., Begelman et al. 1984).

With this justification, we have calculated the flux surfaces in Figure 1 using Equation (8), dropping terms in {...} and taking Equation (6) as a constraint at the disk surface. Note that outgoing flux surfaces at $r < R_0$ are straight, a consequence of the term $\partial^2\Psi/\partial z^2 \propto \partial B_r/\partial z$ in Equation (8) that tends to eliminate B_r in the jet even if B_r were finite at the disk. Here, R_0 is the O-point radius where B_z reverses sign.

The flux surfaces plotted in Figure 1 were calculated using a code called Corsica, which is a GS solver originally developed to understand spheromak magnetic fields like the snapshot in Figure 2 (Hooper et al. 1999). The plasma pressure p was assumed to be small. In Corsica, to apply the boundary condition, we must rewrite the coronal fields in Equations (6) and (7) in terms of the poloidal flux $\Psi(r, z)$ and a quantity $\lambda(r, z)$, defined at the disk by

$$\lambda(r, 0) = (4\pi/c)\big(j_z/|B_z|\big) = |B_z|^{-1}\big(r^{-1}\partial(rB_\phi)/\partial r\big), \quad (9)$$

where on the far rhs we write the current density as $j_z = (c/4\pi)r^{-1}\partial(rB_\phi)/\partial r$.

We obtain λ as a function of Ψ by applying Equation (6) at the disk surface, extrapolated inside the closed flux as in Figure 1(b). Given $\lambda(\Psi)$, the code solves for $\Psi(r, z)$ inside the volume, up to an undetermined magnitude. Otherwise, solutions are uniquely determined by the boundary condition, given by $\Psi = 0$ along the boundary except at the disk surface, where $\Psi(r, 0) = \int_0^r \hat{r}d\hat{r}B_z$ with B_z in Equation (6) at $a < r < R_0$ where this formula applies, then extrapolated in a reasonable way to give a roughly constant B_z at $r < a$, as discussed in Appendix B, and a peak in Ψ at $r = R_0$ and $\Psi = 0$ at $r = R$. To produce Figure 1(a), our $\Psi(r, z)$ compresses the main features of the disk field onto computer grid dimensions, giving the profiles of Ψ, λ, and j_z shown in Figure 1(b). The quantities shown are those halfway up the jet length so as to include the region of closed flux inside the radio lobe, as mentioned above. Since outgoing flux rises vertically (except at the nose), these profiles are also those at the disk, out to the O-point radius R_0 where B_z reverses sign.

The physical argument for large Alfvén velocity can also be seen as follows. It concerns how current is ejected from the accretion disk. Briefly, the disk and jet constitute a single system linked by the magnetic field, much like a Faraday disk that could launch jets in the laboratory as plasma guns do (Fowler 2004). For a Faraday disk, a natural separation occurs at the disk surface where metallic forces cease to provide rigidity, and the continuity of current causes an electrostatic sheath to form so as to eject ions into the jet (the disk is an anode for our sign convention). For accretion disks, also, the cessation of accretion at a height H above the disk serves to separate the disk and jet. The conductivity of the metallic disk is replaced by hyperresistivity $D = -c^{-1}\langle v_1 \times B_1\rangle$ due to disk fluctuations v_1 and B_1, giving as a generalized Ohm's Law (Boozer 1986)

$$E + c^{-1}v \times B = D. \quad (10)$$

The buildup of radial current needed to complete the current loops in Figure 1 is given by D_r inside the disk, given by Faraday's Law $\partial(4\pi j_r/c)/\partial t \approx B_z \partial^2 v_r/\partial z^2$ using $cD_r \approx -cD_\phi \approx v_r B_z$ from Paper I. Thus, the radial current flow j_r

inside the disk is intimately tied to accretion v_r in the disk, both being driven by the same 3D fluctuations inside the disk.

Aside from this different Ohm's Law, accretion disks and Faraday-disk plasma guns share the same requirement to produce a sheath in order to provide particles to carry the current. The density of ejected ions is just that needed to carry the current, perhaps augmented by extra gas beyond the sheath, but altogether yielding a large Alfvén velocity in both the Sustained Spheromak Physics Experiment (SSPX) and jets from accretion disks. The sheath in a gravitational field is discussed in Appendix A.2. Finally, we note that the combination of low jet density and very fast Alfvén velocity in the diffuse pinch avoids bulk flows across critical surfaces encountered in traditional MHD jet models, as well as the light cylinder (see a recent review by Spruit 2010, p. 23).

3.2. Jet Dynamics

As already noted, jet propagation is a competition between momentum equations trying to propagate the jet at Alfvén velocities (v_A), versus Faraday's Law yielding jet power as a Poynting vector that may or may not be able to supply power at the Alfvén rate. At the very low jet densities we have in mind (justified in Appendix A), jet propagation is always power limited, even when Alfvén velocities approach the speed of light. (In this sense, the often-observed superluminal signatures could best be interpreted as the phase speed of disturbances traveling along the jet.) Then speed c never really enters the mathematics. This situation is quite similar to the regime of some laboratory plasma experiments where the Alfvén speed is often orders of magnitude larger than the flow speed. For example, a spheromak formation experiment involves injecting magnetic fields with finite helicity into a metallic tank called a flux conserver, which we regard as similar to astrophysical jets where twisted magnetic fields are "ejected" into a dilute background. Figure 2 shows a nonrelativistic MHD representation of magnetic flux surfaces as fitted to measurements in the SSPX spheromak experiment (Hudson et al. 2008; Hooper et al. 2012). This is a snapshot during the early stage of gun injection into a flux conserver, before reconnection events relax the flux into a spheromak. It turns out that v_A is $\sim 100 dL/dt$ in this experiment, similar to the jet regime derived in Section 3.3.

Furthermore, because $v_A \gg dL/dt$ (where dL/dt is approximately the axial jet speed), the jet remains causally connected to the disk by MHD waves, even as L grows to megaparsec dimensions. As L grows, the field inside is roughly constant in time in the observer's reference frame, except near the nose, thus allowing us to picture jet dynamics as a sequence of equilibria inside an ever-lengthening cylinder. Then the accretion disk voltage V driving the expansion mainly reappears at the nose, with little voltage drop extracting power from the central column. It is this tiny voltage drop $\Delta V \approx 0.01V$ along the column that will account for the low luminosity in the synchrotron and other jet radiations that are the main jet observables (about 1%, Krolik 1999), while most of the action is at the nose, where we will claim UHE cosmic rays are created. This dominance of the nose is another important feature that distinguishes our model from those postulating a significant transfer of magnetic energy to kinetic energy along the way. We will find that even the small power in $I\Delta V$ is exhausted as radiation, not transferred to bulk kinetic energies.

In short, in our model, the central column mainly serves as a causally connected conduit of power from the accretion disk to a cosmic-ray accelerator at the nose of the evolving jet. The main content of this paper is to show how a tower-like jet can maintain collimation, given the known tendency of currents to be violently unstable. We discuss the macroscopic stability of steady-state parameters in Section 3.3, and stability against small perturbations in Sections 4 and 5. Finally, we must reconcile our straight magnetic jet structure with the very different conical picture presented by observations of radiation, discussed briefly in Section 5.2 and more fully in a subsequent paper.

3.3. Calculation of Jet Velocity

In this subsection, we will focus on deriving the jet velocity dL/dt, yielding the jet lengths discussed in Section 6. For this purpose, the large Alfvén velocity giving the rigidity of the GS solution in Section 3.1 allows us to extend the circuit model to the entire jet structure simply by integrating the magnetic energy density inside this structure, without regard to the fact that the circuit model of the central column itself is an approximation to relativistic physics near the black hole (Frank et al. 2002, Chapter 9; see also Appendices B and C).

Then, for the blunt-nosed model in Figure 1, applicable in the fast Alfvén regime $v_A \gg dL/dt$ and valid for radio-loud AGN jets as discussed in Appendix A, the length $L(r)$ from the disk to the nose at radius r can be taken to be independent of r. We will assume the fast Alfvén regime to derive dL/dt for jets from energy conservation, giving

$$\left(1 - f_{\text{conv}}\right)P_{\text{jet}} = \left(1 + F_{\text{shock}}\right)P_{\text{mag}}, \qquad (11)$$

$$P_{\text{mag}} = d\Big/dt\left[\int d\boldsymbol{x}\left(B^2/8\pi\right)\right], \qquad (12)$$

where P_{jet} is the jet power. Thus the power P_{jet} is partly consumed as magnetic energy, partly as the conversion of magnetic energy into kinetic energy with an efficiency f_{conv} through whatever processes, and partly as power in shock waves at the nose, where $F_{\text{shock}} = P_{\text{shock}}/P_{\text{mag}}$.

As it turns out, the jet power $P_{\text{jet}} = IV$, where the current I is the central column current, and the voltage V is the potential difference between $r = a$ and a distant radius $\gg R_0$ where the current returns to the disk. Introducing the dominant component, $B_\phi = (2I/cr)$ in Equation (6), into $B^2/8\pi$ gives

$$\int d\boldsymbol{x}\left(B^2/8\pi\right) = (1/2)\Lambda I^2, \qquad (13)$$

with the inductance Λ given by

$$\Lambda = \left(2L/c^2\right)[1 + \ln(R/a)] \approx \left(2L/c^2\right)\ln(R/a), \qquad (14)$$

where in carrying out the integral we assume the right-circular cylindrical volume of Figure 1 with fixed radius R and length L by the arguments in Section 3.1. As anticipated in Lynden-Bell (2003), the inductance in Equation (14) is mainly that for a quasi-vacuum field due to the central column current filling the diffuse pinch region and radio lobe, though the actual creation of this $\boldsymbol{B}$ field is due to the disk boundary condition, as discussed in Section 3.1. We will take $\ln(R/a) \approx 20$ as representative of the observed radio-lobe radii and the central column radius a. This allows us, on the far rhs, to drop the

unity term representing inductance inside the central column itself.

Note that, while B_ϕ in the diffuse pinch dominates the energy, B_z gives a poloidal flux in the diffuse pinch, generated by the self-excited disk dynamo, that is much larger than the flux through the central column (see Appendix B of Paper I for details).

Our calculation of dL/dt will be further simplified by noting that, after a jet is launched, the current I should hover stably at the minimum current required to eject the jet (the equipartition value, calculated in Section 6). See also Christodoulou et al. (2008). It is sometimes called "bubble burst" in the spheromak literature; see also Li et al. (2001). To see this, we introduce Equations (13) and (14) into Equation (11), giving

$$\frac{\left(1 - f_{\text{conv}}\right)}{\left(1 + F_{\text{shock}}\right)}IV = \frac{d}{dt}\left[\left(\frac{I}{c}\right)^2 L \ln\left(\frac{R}{a}\right)\right]$$

$$= \ln\left(\frac{R}{a}\right)\left(\frac{I^2}{c}\right)\left[\frac{2L}{cI}\frac{dI}{dt} + \frac{1}{c}\frac{dL}{dt}\right]. \qquad (15)$$

This equation is coupled to jet dynamics by Equation (8). Equation (8) by itself would yield a large jet speed $dL/dt \approx v_A \to c$. But in order to satisfy Equation (15), keeping in mind that $cV/I \approx 1$ and $\ln(R/a) \approx 20$, it will require dI/dt at constant V to go negative. Then the current I will fall until it goes below the minimum required for jet ejection. This would eventually interrupt the current, which would soon be restarted, altogether causing the central column current I to hover at equipartition, confirmed by numerical solutions in Fowler et al. (2009a). The same would hold if current were disrupted along the jet, replenished by a "virtual anode" that would form at the point of rupture. Thus we conclude that on time average I is constant. Setting $dI/dt \approx 0$ in Equation (15) gives

$$\frac{dL/dt}{c} \approx \frac{\left(1 - f_{\text{conv}}\right)}{\left(1 + F_{\text{shock}}\right)}\frac{1}{\ln(R/a)}, \qquad (16)$$

where on the rhs we have approximated $cV/I \approx 1$ to give $dL/dt \leqslant c$ for no shock and zero dissipation.

Next we estimate the shock heating contribution. By the arguments above, the magnetic piston driving shocks is a relatively rigid structure with maximum pushing power P_{mag} in Equation (12). Because dL/dt will turn out to exceed the ambient sound velocity, the Rankine–Hugoniot equations predict that the magnetic piston produces a strong shock in the ambient with back pressure $p_{\text{shock}} \approx (1/2)[(\Gamma + 1)/(\Gamma - 1)]\rho_{\text{AMB}}(dL/dt)^2$ with adiabatic gas Γ (Harris 1975), requiring a piston pushing power $P_{\text{shock}} = dL/dt\ (\pi R^2 p_{\text{shock}})$. Here we will take $P_{\text{shock}} \approx P_{\text{mag}}$, to be justified by jet numbers derived in Section 6. Then

$$F_{\text{shock}} = P_{\text{shock}}/P_{\text{mag}} \approx 1. \qquad (17)$$

We now substitute $F_{\text{shock}} \approx 1$ into Equation (16), using $\ln(R/a) \approx 20$, and anticipating results in future papers, $(1 - f_{\text{conv}}) \approx 1/2$. We obtain

$$dL/dt \approx 0.01c. \qquad (18)$$

The observational implications of Equation (18) are discussed in Section 6.

We note that Equation (18) giving $dL/dt \ll c$ is quite general, being equivalent to

$$dL/dt < f(1/4)\dot{M}c^2 \left\{ \int_{JET} dx \left[\left(B^2 + E^2\right)/8\pi \right] \right\}^{-1}$$
$$< f(1/4)\dot{M}c^2 \left\{ \int_{JET} dx \left[\left(B_\phi^2 + B_z^2\right)/8\pi \right] \right\}^{-1}, \quad (19)$$

where, if E and B are mean fields, the first inequality represents the missing hyperresistivity and other dissipative processes, applicable also to the GRMHD simulations discussed in Appendix C.

4. JET STABILITY: LINEAR THEORY

As discussed in Section 2, we can anticipate that jets carrying current are unstable, our main interest being the nonlinear consequences of instability, to be discussed in Section 5. Here we first characterize instabilities using well-known linear theory. In this section we consider only the diffuse pinch zone of our jet model, where magnetic mean fields describing the equilibrium state are well-characterized in Equation (6). We will extrapolate these results into the central column in Section 5.

Pressure being negligible in our jet model, the instabilities of interest are the kink modes occurring if twisting field lines in three dimensions lower the inductance. For these modes, we can establish the existence of instability in the diffuse pinch, where the electric field $E \ll B$, using the nonrelativistic Energy Principle as formulated for very long pinches with periodic boundary conditions, even though the physical boundary might fix fields in the disk (see also Huang et al. 2006; Delzanno et al. 2007; Carey et al. 2011). Thus we assume $k = (m/r, k_z)$ for perturbations $\propto \exp i\{-\omega t + (m/r)\phi + k_z z\}$; we represent the current as λ from Equation (9). We first write the energy change δW in the diffuse pinch in the form usually employed in ideal MHD theory, giving

$$\frac{\delta W}{2\pi L} = \int_a^{R_v} r\,dr\,c^{-1}\boldsymbol{\xi} \cdot \left(\boldsymbol{j}_1 \times \boldsymbol{B} + \boldsymbol{j} \times \boldsymbol{B}_1\right) \quad (20a)$$

$$= \int_a^{R_v} dr \left\{ HF^2\xi'^2 + g_E\xi^2 \right\}, \quad (20b)$$

where $\boldsymbol{\xi}$ is a 3D displacement of a field line and $(') = d/dr$. The derivation of Equation (20b) is somewhat involved. We follow Freidberg (2014), who followed Newcomb (1960), but with the notation in Furth et al. (1973), giving, with $k \equiv k_z = (2\pi/L)n$,

$$H = r^3 / \left(k^2 r^2 + m^2\right), \quad (21a)$$

$$F = \boldsymbol{k} \cdot \boldsymbol{B} = k_z B_z + (m/r)B_\phi$$
$$= (2\pi/L)B_z(n - m/q), \quad (21b)$$

$$g_E = \left(k^2 r^2 + m^2\right)^{-1} \Big\{ \left(m^2 - 1 + k^2 r^2\right) rF^2$$
$$+ \left[\left(2k^2 r^2 F\left(krB_z - mB_\phi\right)/\left(k^2 r^2 + m^2\right)\right) \right] \Big\}$$
$$= \frac{B_\phi^2}{r\left(k^2 r^2 + m^2\right)} \Big\{ \left(m^2 - 1 + k^2 r^2\right)(nq - m)^2$$
$$+ \frac{2k^2 r^2}{k^2 r^2 + m^2}\left(n^2 q^2 - m^2\right) \Big\}, \quad (22)$$

$$q = \left(2\pi r B_z\right)/\left(LB_\phi\right). \quad (23)$$

In order to treat "tearing" kink modes involving reconnection of field lines, following Rosenbluth & Rutherford (1981) we generalize the displacement ξ as

$$\xi = A_{1z}/(rF). \quad (24)$$

Substituting Equation (24) into Equation (20b) gives

$$\delta W = \int_a^{R_v} \frac{dr}{r}\left\{ \left(rA_{1z}'\right)^2 + A_{1z}^2\left[m^2 - \frac{(mrB_z)}{(\boldsymbol{k} \cdot \boldsymbol{B})}\lambda' \right] \right\}, \quad (25)$$

where λ is given in Equation (9). Other terms not important here are given in Robinson (1978). Ideal modes with finite ξ are recovered if $A_{1z} = 0$ at magnetic resonances where $\boldsymbol{k} \cdot \boldsymbol{B} = 0$, but Equation (25) also includes tearing modes. Since Equation (25) only involves Maxwell's equations, it is nonrelativistic only in that the electric force $(\nabla \cdot \boldsymbol{E}/4\pi)\boldsymbol{E}$ is not perturbed, valid in the diffuse pinch where $E \ll B$. We will deal with E in the central column in Section 5.

We search for instability by introducing appropriate trial functions for A_{1z} into δW. An unstable mode is indicated if $\delta W < 0$. The key is to pay close attention to resonances in choosing trial functions. Resonances occur if q in Equation (23) is a rational number.

We first consider tearing modes, for which δW in Equation (25) can be simplified as follows. Following Hegna & Callen (1994), applied also in Fowler et al. (2009b), we expand $\boldsymbol{k} \cdot \boldsymbol{B}$ around the resonance at $r = r_0$ using Equation (21b). We obtain

$$1/q = n/m + (1/q)'(r - r_0) + ..., \quad (26a)$$

$$\boldsymbol{k} \cdot \boldsymbol{B} = (2\pi/L)B_z(n - m/q)$$
$$\approx (2\pi/L)B_z m(1/q)'(r_0 - r), \quad (26b)$$

$$\lambda = r^{-1}\left[\left(\partial(rB_\phi)/\partial r\right)/B_z \right] = (1/2a)(a/r)^{3/2}, \quad (26c)$$

$$1/q = (L/2\pi)/(ar)^{1/2}. \quad (26d)$$

Substituting Equation (26b) into Equation (25) with $(r - r_0) \approx r$ over most of the domain of interest, we obtain

$$\delta W = \int_a^{R_v} \frac{dr}{r}\left\{ \left(rA_{1z}'\right)^2 + A_{1z}^2\left[m^2 - \frac{\lambda'}{(1/q)'}\frac{L}{2\pi} \right] \right\}. \quad (27)$$

Then δW is certain to be negative, indicating instability if we choose A_{1z} to minimize the effect of A_{1z}' and we require

$$\frac{\lambda'}{(1/q)'}\frac{L}{2\pi} = (3/2)(a/r) > m^2 > 1. \quad (28)$$

This means that the tearing instability occurs, but only at $r/a < 3/2$ in the neighborhood of the central column and only if $m = 1$.

Next we consider ideal modes by choosing A_{1z} to give ξ in Equation (24) that is constant so as to eliminate the positive contribution of ξ' in δW as written in Equation (20b). This δW is the change in energy where $\xi(r)$ is concentrated, inside a radial zone $r \leqslant R_v$ containing the jet. There is some ambiguity in deciding R_v, to which we return at the end of this section. Roughly, one can take $R_v = R_0$, the O-point radius that defines the edge of the diffuse pinch zone. Let $r < R_1 \leqslant R_v$ be the volume of interest. Then for R_1 in the jet interior, eliminating

the ξ' term in δW requires terminating ξ at a resonance over a small width Δ. Then for the first term in Equation (20b), we obtain a contribution only around the resonance where $\xi' \approx \xi/\Delta$, and we can expand $F = \Delta F'$, giving

$$\int_a^{R_1} dr H F^2 \xi'^2 \approx \Delta H |\Delta F'(\xi/\Delta)|^2 \propto \Delta \to 0. \qquad (29)$$

By Equation (20b), instability is determined by integrating g_E over the range $r \leqslant R_1$ where the field line displacement ξ is nonzero, with $q(R_1) = m/n$ at the resonance. Instability requires $\int_0^{R_1} dr g_E < 0$. Near resonance, $q = (m/n)(1 - \epsilon)$ gives $(nq - m)^2 = \epsilon^2 (m/n)^2$, while $(n^2 q^2 - m^2) = 2\epsilon (m/n)^2$, which always leads to $g_E < 0$ for ϵ sufficiently small. But this makes only a small contribution to $\int_0^{R_1} dr g_E$, so to a good approximation we can take $nq \ll m$. With this approximation, Equation (22) gives $g_E \propto (m^2 - 1 + k^2 r^2) - 2k^2 r^2 / (k^2 r^2 + m^2)$, which is positive for all kr if $m \geqslant 2$. Thus instability requires $m = 1$. For $m = 1$, we can obtain $g_E = -r B_\phi^2 k^2 N(r)$, where $N(r) = (1 - k^2 r^2)/(1 + k^2 r^2)^2$. When $kr < 1$, we get $N(r) > 0$ but $g_E < 0$. Negative g_E gives negative δW_P, which leads to instability. Expanding $N(r)$ in powers of $k^2 r^2$ and using also B_ϕ in Equation (6), we obtain for the diffuse pinch free energy

$$\frac{\delta W}{2\pi L} \approx \int_a^{R_1} dr g_E \xi^2$$
$$\approx -B_a^2 k^2 a^2 \xi_a^2 \Big[\ln(R_1/a) - (3/2)k^2 (R_1^2 - a^2) \Big], \quad (30)$$

where $\xi = \xi_a$ is taken as constant for the reasons given above. The maximum $|\delta W|$ gives the greatest growth rate. It can be found by maximizing on k at fixed R_1. This yields, by Equation (30)

$$k^2 a^2 = \ln(R_1/a) \Big/ \Big\{ 3\big[(R_1/a)^2 - 1 \big] \Big\}, \qquad (31a)$$

$$\frac{\delta W}{2\pi L} = -B_a^2 \xi_a^2 \Big\{ \ln^2(R_1/a) \Big/ \big[6\big(R_1^2/a^2 - 1\big) \big] \Big\} \text{ (internal)}. \qquad (31b)$$

Maximizing δW on R_1 gives $R_1/a \approx 2.2$, which leads to $ka \approx 0.26$. Thus, as for tearing modes, we find that ideal trial functions confined to the interior of the jet only give instability for $ka \sim O(1)$, indicating instability is localized to the neighborhood of the central column. That is, this class of kink modes is localized, meaning that it does not destroy collimation of the jet.

We will refer to these localized modes as internal kinks. That ideal internal modes are localized in this way has been further verified by numerical calculations of δW for a force-free equilibrium with $B_z \approx B_a/[1 + (r/a)^{3/2}]$, mentioned in Appendix B as a way to extend the diffuse pinch solution in Equations (6) and (7) into the central column. This result obtained from δW has been further verified by direct ideal MHD mode analysis for this equilibrium, using the nonlinear Gyrokinetic Toroidal Code (GTC; Deng et al. 2012; McClenaghan 2015) but dropping nonlinear terms. Linearized GTC results are shown in Figure 3. Figure 3 (left) shows that the growth rate γ is maximum near $k_z a = 1$, as expected. Figure 3 (right) shows that the electric potential perturbation $\delta\phi$ is maximum near $r = a$, again as expected.

By extending $R_1 \to R_v$ as defined in Equation (20b), we can also apply Equation (30) to modes with very long wavelengths such that k is small enough to avoid all resonances, giving for k giving $N(r) \approx 1$

$$\frac{\delta W}{2\pi L} = -k^2 a^2 B_a^2 \xi_a^2 \ln(R_v/a) \text{ (external)}. \qquad (32)$$

We will call these long wavelength modes "external" modes to distinguish them from the "internal" modes to which Equation (31b) applies.

There is some ambiguity in choosing R_v. First, sufficient plasma may exist everywhere inside the return-current boundary in Figure 1 so that all of this volume is part of δW. Second, the contribution of distant resonances to δW where B_ϕ is small is so weak that, at some large r, we can let ξ begin to fall off gently enough that $HF^2\xi'^2$ makes a negligible contribution to δW, thus allowing us to terminate ξ inside R_v so that there is no contribution from outside. Finally, even if we treat $r > R_v$ as a literal vacuum, it turns out that the vacuum response, given in Freidberg (2014) as $\delta W_E/(2L) = (k\xi r B)_{R_v}^2 \approx (k\xi_a a B_a)^2$ for an infinitely distant outer wall, though stabilizing, still gives instability due to the large logarithmic factor above. Noting that all jet power is ejected at $r < R_0$, the O-point radius, for practical purposes, we will choose $R_v = R_0$, giving $kR_0 \leqslant 1$ as the range of wavenumbers for unstable external modes.

5. JET TURBULENCE: NONLINEAR DEVELOPMENT

The most important result in Section 4 is our finding that current-driven instability in our AGN jet model cleanly divides into "internal" short-wavelength modes with $k_z a \approx 1$ confined to the neighborhood of the central column in Figure 1, and very long wavelength "external" modes with $k_z R_0 < 1$ corresponding to a rigid displacement of the entire jet structure. This division of kink modes into internal and external modes is also consistent with the previous nonrelativistic magnetic tower jet simulations (Nakamura et al. 2007, 2008) and with the recent relativistic simulations (Bromberg & Tchekhovskoy 2015). Here the importance of this finding lies in the fact that it will turn out that the short-wavelength internal modes can accelerate cosmic ray ions without destroying the jet, while the long-wavelength external modes provide the power emitted as synchrotron radiation by which jets are observed.

Evaluating the importance of instabilities discussed in Section 4 requires estimating their nonlinear effects as amplitudes grow, either steadily for slowly growing modes, or to a point of saturation for fast modes. In the spirit of this paper, we will uncover some important nonlinear effects not yet adequately explored in simulations that we hope will serve as a guide to future work.

5.1. Nonlinear Development of Internal Kink Modes

As noted above, at saturation, internal kink modes accelerate ions while preserving the integrity of the jet. Concerning jet integrity, internal kink modes only disturb the jet current near the central column, while external modes have such long wavelengths that they only develop over the observed length of jets (see Section 5.2). Concerning particle acceleration, while the electric field parallel to **B** is strictly zero in ideal 3D MHD, correlations in perturbations $\mathbf{E}_1$ and $\mathbf{B}_1$ can produce, even for ideal kinks, a nonzero value for the electric field
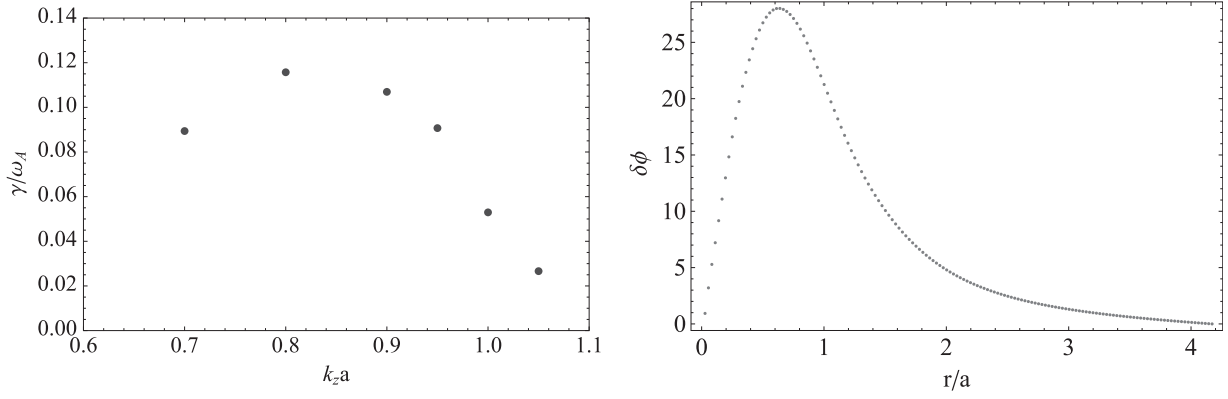
Figure 3. Results of linearized simulations of internal kink modes. Left: the growth rates are plotted for modes of different normalized axial wave number $k_z a$, where a is the central column radius. Right: the mode structure of the electrostatic potential $\delta\phi$ with $k_z a = 0.9$ plotted versus radius r. The peak occurs near $r = a$.

$E_\parallel = -\langle (E_1 \times B/B) \times B_1 \rangle_\parallel$ averaged over ϕ. It is this $E_\parallel$ that accounts for ion acceleration in the Spheromax Experiment (SPHEX) (Rusbridge et al. 1997), discussed in Section 7.

Pending further progress on general relativistic MHD codes discussed in Section 8 and Appendices B and C, the nonlinear transport rates discussed in this section must rely on simple estimates. Here we follow the fully nonlinear free-energy method of estimation corresponding to δW in linearized MHD theory but also applicable to all processes included in the Vlasov equation (see, e.g., Fowler 1968, p. 201). Using this method, we can determine upper limits on the nonlinear effect of internal kink modes as follows.

We assume that internal kinks develop in a fixed radial domain $0 < r < R_1$ for some $R_1 \ll R_0$, justified by the fact that internal kinks are either localized near a magnetic resonance (tearing) or terminate there (ideal modes). We can then set rigorous limits on the radial extent of mode activity, indicating that internal mode turbulence does not destroy collimation.

As for the linear stability analysis in Section 4, we can describe the radial extent of turbulence using either a line displacement ξ (as in MHD theory) or a field perturbation, the two being related by Rosenbluth & Rutherford (1981):

$$\xi = \frac{A_{1z}}{r \boldsymbol{k} \cdot \boldsymbol{B}} \approx r\left(\frac{B_{1r}}{B_\phi}\right), \tag{33}$$

where on the far rhs we use $B_{1r} = (m/r)A_{1z}$ and, to explore displacements away from exact resonance, we approximate $\boldsymbol{k} \cdot \boldsymbol{B} \approx (mB_\phi/r) = B_\phi/r$ for the dominant field component and the dominant instability mode $m = 1$. Following Fowler (1968, p. 201), we can set upper limits on B_{1r}/B_ϕ by bounding the free energy available by relaxation at constant entropy, which, for MHD, is the global magnetic helicity $K = \int dx A \cdot B$, giving $\nabla \times B = \lambda B$ with constant λ_0 as the relaxed state of minimum energy (Taylor 1986). For the relaxed state, $B = \nabla \times A = \lambda A$ gives $\lambda K/8\pi$ as the relaxed energy. At constant helicity, K is also that in equilibrium, yielding the free energy ΔE given by

$$\Delta E = E - \lambda_0 K/(8\pi)$$
$$= (1/4)L \int_0^{R_1} r\,dr\,\boldsymbol{B} \cdot (\boldsymbol{B} - \lambda_0 \boldsymbol{A}), \tag{34a}$$

$$\approx (1/4)La^2B_a^2 \Big\{ 1 + \ln(R_1/a) + 2\big[2\ln(R_1/a)$$
$$- 4\big((R_1/a)^{1/2} - 1\big)\big]\Big\}. \tag{34b}$$

Here $\boldsymbol{B}$ and $\boldsymbol{A}$ are the equilibrium fields in Equation (6) with dominant components $B_\phi \approx B_a(a/r)$ and $A_\phi = 2aB_a(a/r)^{1/2}$ chosen to give B_z in Equation (6). Substituting these dominant field components into Equation (34a) gives Equation (34b), using also $\lambda_0 a \approx 2$ derived as follows. To the lowest order, the relaxed $B_\phi = B_z(0)(\lambda r/2)$, giving $B_\phi(R_1) = B_z(0)(\lambda R_1/2) = B_a(a/R_1)$ (since fields are not disturbed there), from which $\lambda R_1/2 \approx \lambda a/2 \approx 1$ is the ratio of equilibrium and relaxed poloidal fluxes, which are equal since A_ϕ is not perturbed at the boundary either.

The free energy in Equation (34b) becomes negative (stability) for R_1/a much above unity, while $\Delta E \approx (1/4)LR_1^2 \langle B_1^2 \rangle = (1/4)La^2B_a^2$ for $R_1 = a$, with corresponding excursion $\xi = a(B_{1r}/B_\phi) \approx a$. This estimate is consistent with the speculative magnetic field profiles at $r < a$ in Appendix B, and the corresponding electric field energy is at most comparable to the magnetic energy. Then, for internal modes, $\xi \leqslant a$ is confined to the active zone $R_1 \approx a$. Note that for internal modes within a fixed resonance at $r = R_1$, ΔE above is a nonlinear limit on the quasi-linear δW_P in Equation (30), giving similar results for $k^{-1} \approx \xi \approx a$. Nonlinear 3D relativistic MHD simulations of magnetically driven jets show relatively short wavelength kink modes in the central region along the jet axis, consistent with the analysis here (Guan et al. 2014).

5.2. Nonlinear Development of External Kinks: Wandering Field Lines

External modes with much longer wavelengths persist by perturbing the boundary outside all resonances. Nonlinear 3D nonrelativistic MHD simulations of jet+lobe systems on the largest scale (e.g., jet+lobe sources in galaxy clusters as described in Li et al. 2006) have produced morphologies that are consistent with this expectation (e.g., Nakamura et al. 2006, 2007, 2008). In this section, as noted earlier, we are mainly interested in external kinks as conduits of power observed as synchrotron radiation. Since the disk Poynting power $\propto r\Omega B_z B_\phi \propto r^{-3}$ by Equation (6) with Keplerian rotation, most of the power emerges at $r < a$, suggesting that

we concentrate on the wandering of field lines emanating from this region of the disk corona. This is our example of a nonlinear effect not yet properly modeled in MHD codes, and not in GRMHD codes either since they do not include the acceleration of ions that we find to be the crucial point. This is also an example of a conceptually clear phenomenon that nonetheless is beyond simple calculation. Thus we resort to a heuristic model of wandering field lines.

Since the wandering of field lines is a dynamic process, we can no longer consider only energy changes but must also consider growth rates along the jet. As for internal modes, we can use as the measure of line wandering the field line displacement in Equation (33). In nonrelativistic theory, initially ξ grows as $d\xi/dt = \omega\xi$. The initial growth rate is order $\omega \approx k v_A$ (Alfvén velocity) according to theoretical results in Cohen et al. (2009) calibrated to the SSPX experiment mentioned in Section 3.2. For jets with an extended diffuse pinch, $\omega = \left(\delta W / \int d\mathbf{x} \rho \xi^2\right)^{1/2} \approx [\ln(R_0/a)]^{1/2} k_z v_A$.

Rutherford (1973) showed that the linearized exponential growth of kink modes ceases as soon as the nonlinear island width exceeds the linearly calculated resonance width, after which growth is secular $\propto t$. Here we will show that external mode growth saturates by a different process, again yielding secular growth. The reason concerns the acceleration of ions parallel to $\mathbf{B}$ and how this affects the Alfvén velocity. As we noted in the Introduction, this acceleration ultimately yielding UHE cosmic rays is a kinetic process not included in relativistic MHD simulations and not readily calculated analytically, forcing us to resort to rough approximations. Why the growth becomes secular due to relativity can be seen as follows. We assume $\omega \propto v_A$ as in linear theory, giving

$$d\xi/dt = \omega\xi = (\gamma_0/\gamma_L)^{1/2}\omega_0\xi. \quad (35)$$

Here ω_0 is the Alfvénic growth rate with Lorentz factor $\gamma_0 = (1 - v^2/c^2)^{-1/2}$, where $\mathbf{v}$ is the average velocity of ions accelerated along wandering field lines, while γ_L includes the randomly directed $\omega\xi$, giving $\langle(\mathbf{v} + \omega\xi)^2\rangle = v^2 + (\omega\xi)^2$. We obtain

$$\gamma_L = \left[1 - \left(v^2 + (\omega\xi)^2\right)/c^2\right]^{-1/2}$$
$$= \gamma_0/\left[1 - \chi(\gamma_0/\gamma_L)^{1/2}\right], \quad (36a)$$

$$\chi = (\gamma_0\omega_0\xi/c)^2. \quad (36b)$$

where on the far rhs of Equation (36a) we use $\omega = (\gamma_0/\gamma_L)^{1/2}\omega_0$ as in Equation (35). Equation (36a) is a quadratic equation in γ_0/γ_L. Solving for it gives $\gamma_0/\gamma_L = 1/2[-\chi + (4 + \chi^2)^{1/2}]$, and substituting this into Equation (35) gives

$$d\xi/dt = \omega_0\xi, \quad \chi \ll 1 \quad (37a)$$
$$= \omega_0\xi/\chi^{1/2}, \quad \chi \gg 1. \quad (37b)$$

Thus the secular growth sets in when exponential growth gives $\chi > 1$. This happens early in the jet evolution, giving after an elapsed time t

$$\xi \approx (c/\gamma_0)t. \quad (38)$$

We interpret Equation (38) as follows. As noted above, most of the power flow along wandering field lines enters the tangled field near $r = a$ and only wanders radially as ξ grows along z. The dotted cone in Figure 1 bounds the path of these wandering

lines, with an opening angle Θ given by

$$\Theta \approx \xi(z)/z = (c/\gamma_0)t/z = 100/\gamma_0, \quad (39)$$

where we take t to be the elapsed time required for the jet to extend to a height z, giving $t = z/(dL/dt) = 100z/c$ by Equation (18).

6. PREDICTED DIMENSIONS OF THE JET MAGNETIC STRUCTURE

We start this section with a review of needed jet parameter values derived from our circuit model for the central column using results from Paper I, summarized as follows. We describe the central column by the power it carries, given in terms of the central column current I and voltage V by

$$IV = f\left(\dot{M}c^2/4\right), \quad (40)$$

where f is the efficiency for converting gravitational power into Poynting power. In this, we follow many authors (e.g., see the review by Beskin 2010 and a textbook summary of applications to pulsars in Frank et al. 2002, Chapter 9). The main difference in our work is how we couple Equation (40) to the Poynting vector to find also the central column radius a, rotation frequency Ω_a, and field B_a, whereby our separation into a diffuse pinch zone and the central column pins down numbers left uncertain in previous work. We do this by finding simultaneous solutions of Equation (40) with Equation (5) and by considering the fact that $B_z(a) = B_\phi(a) = B_a$ for the exact calculation of diffuse pinch fields in Paper I. We obtain the following parameters:

$$a\Omega_a/c = (R_s/2a)^{1/2} = (f/b)^{1/2} \approx 0.2, \quad (41)$$

$$a = (b/2f)R_s = 10R_s = 3 \times 10^{14}M_8 \text{ cm}, \quad (42)$$

$$B_a = \left(\dot{M}\Omega_a/2a\right)^{1/2} \approx 1.5 \times 10^3 M_8^{-1/2} \text{ Gauss}, \quad (43)$$

$$I = \left(aB_ac\right)/2 \approx 0.7 \times 10^{28}M_8^{1/2} \text{ statamp}, \quad (44)$$

$$V = b\left(a\Omega_a/c\right)aB_a \approx (2I/c) \approx 0.5 \times 10^{18}M_8^{1/2} \text{ statvolt}, \quad (45)$$

where $M_8 = M/(10^8 M_{\text{Sun}})$ and $R_s = 2GM/c^2 \approx 3 \times 10^{13}M_8$ cm; we have also taken $\dot{M} = M/\tau$ for a typical system lifetime of $\tau = 10^8$ yr (e.g., Colgate & Li 2004; Beskin 2010). The current I is the central column current; $V = b\Phi(a)$ where $\Phi(a)$ is the potential difference between $r = a$ and a distant radius $\gg R_0$ where the current returns to the disk. The coefficient b is an average enhancement of $\Phi(r)$ over the central column.

This completes our model aside from the parameters f and b. The numbers on the far rhs assume $f = 1/4$, derived in Paper I as an extrapolation of the calculated efficiency on flux surfaces in the diffuse pinch zone. The parameter $b = V/\Phi(a)$, taken as 5, is more uncertain, but $V = b(a\Omega_a/c)aB_a \propto b(b^{-1/2})(b^{-1/4}) = b^{1/4}$ is only weakly dependent on b. Of greater concern is whether a quasi-steady solution actually exists at $r < a$, given the fact that codes including the black hole region do not yet obtain the straight collimated jets predicted by our model, as discussed in Section 8. We discuss this issue in Appendices B and C, with the conclusions that a collimated jet can be consistent with black hole physics, and $b = 5$ is a reasonable value.

Note that these values also yield $cV/I = 2(fb)^{1/2} \approx 1$, as we assumed in deriving dL/dt by Equation (18). Also, we can now examine our approximation $F_{\text{shock}} \approx 1$ used in that derivation. We obtain

$$
\begin{aligned}
F_{\text{shock}} &= P_{\text{shock}}/P_{\text{mag}} \\
&= 2\rho_{\text{AMB}}(dL/dt)^2 \big/ \big[2\ln(R/a)B(R)^2/8\pi \big] \\
&\sim 10^3[(dL/dt)/c]^2,
\end{aligned} \tag{46}
$$

where on the first line we introduce $P_{\text{shock}} = A(dL/dt)[2\rho_{\text{AMB}}(dL/dt)^2]$ with $\Gamma = 5/3$ from the discussion in Section 3.3 with a radio-lobe area $A = \pi R^2$, and $P_{\text{mag}} = A(dL/dt)[2\ln(R/a)B(R)^2/8\pi]$ obtained by inserting $B_\phi(R) \approx (a/R)B_a$ from Equation (6) into Equation (12). The second line is obtained taking also $a/R \approx 10a/L \approx 3 \times 10^{-9}$ and B_a from Equation (43); $\rho_{\text{AMB}} = 1.7 \times 10^{-29}$ gm cm^{-3} for hydrogen with number density 10^{-5} cm^{-3} (Colgate & Li 2004). Introducing Equation (40) into Equation (16), still with $f_{\text{conv}} = 0.5$ and $\ln(R/a) = 20$, we obtain $(dL/dt)/c = 0.018$ for $M_8 = 1$, compared to $(dL/dt)/c \approx 0.01$ in Equation (18). For a nominal ambient temperature of 1 KeV, the sound speed at this density is $c_S/c \approx 10^{-3}$, thus justifying the assumption of a fast shock in Section 3.3.

6.1. Jet Length and Radius

In our model giving the 2D mean field in Figure 1, we must carefully distinguish between the magnetic mean field structure and the apparent shape of jet structures associated with synchrotron images in radio lobes. Our prediction of the visible length L of the jet is just the length of the magnetic structure derived in Section 3. Our prediction for the radius is loosely the diffuse pinch radius R_0 (O point), which is the outer radius of Poynting power ejected from the disk, visible only as the terminal radius of a bright cone illuminated by synchrotron radiation with opening angle Θ given by Equation (39).

Growth of the column length L should continue for a time $\tau \approx 10^8$ years, observed to be the lifetime of jet/lobes independent of mass (e.g., Krolik 1999; Colgate & Li 2004), perhaps related to the Eddington radiation limit (Beskin 2010). Using Equation (18), we obtain

$$
L \approx (dL/dt)\tau = 0.01c\tau \approx 10^{24} \text{ cm.} \tag{47}
$$

Next we derive the diffuse pinch radius R_0 in Figure 1. While L is the main dynamical variable, we expect that R_0 also grows but more slowly. As was discussed in Appendix B of Paper I, why R_0 grows is related to how hyperresistivity due to 3D magnetic fluctuations can defeat Cowling's antidynamo theorem in 2D, through the intervention of a helicity-conserving hyperresistivity $\mathcal{D}_\phi$ in $\partial\Psi/\partial t + \mathbf{v} \cdot \nabla\Psi = rc\mathcal{D}_\phi$. A formula for a helicity-conserving $\mathcal{D}_\phi$ in terms of correlated fluctuations was given in Paper I. Here we avoid needing to know fluctuations by approximating $c\mathcal{D}_\phi$ as

$$
c\mathcal{D}_\phi = |\Psi|/(r\tau) - |v_r||B_z| \tag{48a}
$$

$$
|\Psi| = \int_a^r r\,dr\, |B_z| = 2B_a a^{3/2} r^{1/2}. \tag{48b}
$$

where we use B_z from Equation (6). Noting that $c\mathcal{D}_\phi \approx -|v_r||B_z| < 0$ below the O point but flux growth requires $c\mathcal{D}_\phi > 0$ at the O point where $B_z = 0$, we see that $c\mathcal{D}_\phi$ changes sign at some $R_1 < R_0$. We calculate R_1 by substituting

$|B_z(R_1)|$ from Equation (6) and $|\Psi(R_1)|$ from Equation (48b) into Equation (48a) and solving with $c\mathcal{D}_\phi = 0$. Also taking $R_1 = R_0/\alpha_z$ with an uncertain factor $\alpha_z < 1$, we obtain

$$
\begin{aligned}
\frac{R_0}{L} &= \left(\frac{t}{\tau}\right)^{2/3}\left(\frac{a}{L}\right)^{1/3}\left(\frac{c\tau}{10L}\right)^{2/3}\alpha_z \left|\frac{v_r}{v_\phi}\right|^{2/3} \\
&\rightarrow 0.003 M_8^{1/3}\alpha_z \left|\frac{v_r}{v_\phi}\right|^{2/3}.
\end{aligned} \tag{49}
$$

The far rhs is the result at $t = \tau = 10^8$ years (e.g., Colgate & Li 2004; Beskin 2010), the typical jet lifetime.

Our predicted length $L = 10^{24}$ cm (0.3 Mpc) in Equation (47) is reasonably consistent with observations for jet/lobes associated with radio-loud AGNs (Begelman et al. 1984; Krolik 1999).

Concerning the diffuse pinch radius R_0, we note that the persistence of a 2D jet with fixed R_0 is the expected consequence of current conservation in our model. As in the simulations of Nakamura et al. (2006, 2007), weak instability in three dimensions creating the radio lobes does not destroy the 2D projection giving a collimated jet that nonetheless produces field lines wandering into the radio lobe, by Equation (39). We assume that it is synchrotron radiation that defines the observed structure of jet/lobes (the dotted cone in Figure 1), rather than the underlying magnetic mean field structure in Figure 1. As already noted, the power radiated as synchrotron radiation is transmitted from the mean field central column by nonlinear external kink modes producing twisted field lines. Typical AGN jet envelopes exhibit large, fuzzy radio lobes emerging from a very bright conical streak that appears to originate near the black hole with an opening angle of order $\Theta \approx 0.01$ radians. This is consistent with Θ as derived in Equation (39) if we take $\alpha_z |v_r/v_\phi|^{2/3} \approx 0.4$, giving

$$
\frac{R_0}{L} \approx 0.001, \tag{50}
$$

with our undetermined ordering parameter in Paper I equal to $|v_r/v_\phi| \approx 0.01$ for $\alpha_Z = 10$, showing consistency with our assumption that $|v_r/v_\phi| \ll 1$ in the diffuse pinch zone of the accretion disk.

6.2. Predicted Light Cone

We conclude this section with an evaluation of the opening angle Θ in Equation (39), which we interpret as the opening of 3D jet emission cones illuminated by synchrotron radiation due to that half of the power going into electrons. To evaluate Θ, we estimate γ_0 at z from the ion energy acquired by acceleration, but ignoring radiation for now (see below). We assume an accelerating field on axis $E_{\text{axis}} = 0.01(V/L)$, giving $\gamma_{\text{MAX}} = 0.01 \text{ eV}/m_i c^2 = 1.5 \times 10^9 M_8^{1/2}$ with V from Equation (45), where 0.01 is the fraction of Poynting power going into synchrotron emission, as derived in subsequent papers in rough agreement with observations (Krolik 1999). We further assume that ions follow the path of wandering field lines approximated as $r(s) < z\Theta < z(R_0/L)$ with the O-point radius R_0, and we take the accelerating field to be $E_s = E_{\text{axis}}a/r(s)$

along this path. Then, we get

$$
\gamma_0 = \int_a^L ds \left(eE_s/m_i c^2 \right) = \gamma_{\mathrm{MAX}} \int_a^L ds \, (1/L)[a/r(s)]
$$
$$
> \gamma_{\mathrm{MAX}} \int_a^L dz \, a \Big/ (zR_0),
$$
(51)

$$
\Theta \approx (100/\gamma_0) = 100 \left[\gamma_{\mathrm{MAX}} \int_a^L dza \Big/ (zR_0) \right]^{-1}
$$
$$
< 10 (R_0/L) M_8^{-3/2} \approx 0.01,
$$
(52)

with the O-point radius R_0 in Equation (50). Using numbers in Equations (41)–(45), we write the integral as

$$
\int_{z_0}^L dz \, a/(zR_0) = (a/R_0)\ln(L/a) \approx 20 (a/R_0)
$$
$$
= \left[20 \Big/ \left(3 \times 10^9 M_8 \right) \right] (L/R_0)
$$
(53)

for any starting point for the integration $z = z_0$ near the disk, which we take to be $z_0 = a$ with little error since z_0 enters only logarithmically.

Note that in calculating γ_0 we have omitted radiation by ions, which will be dealt with extensively in future papers but is not important here. First, ions tend to radiate away any velocity component perpendicular to $\boldsymbol{B}$. That leaves curvature radiation as ions try to follow twisting field lines, important in the tightly wound central column, but not important along the path of wandering field lines where the field line curvature radius becomes comparable with the O-point radius.

We postpone a detailed comparison with synchrotron observations to subsequent papers. Understanding the distribution of synchrotron emission along the z axis and the synchrotron frequency spectrum will require other nonlinear effects due to coupling of $m = 1$ modes to higher m modes (e.g., Carey et al. 2011). But the visible cone defined by Θ is unaffected, the nonlinear evolution of Θ being independent of ω, as derived in Equation (39).

7. EVIDENCE FOR THE MODEL FROM OBSERVATIONS, EXPERIMENTS, AND SIMULATIONS

The most direct vindication of our quasi-static model of jets is the extreme length of jets in Equation (47), in rough agreement with observations. In subsequent papers, we suggest that the nonrelativistic jet velocity giving this result can be reconciled with observations interpreted as relativistic jets as being the effects of relativistic acceleration of ions and electrons parallel to $\boldsymbol{B}$.

The best evidence that the short-wavelength internal kink modes in Section 4 could accelerate ions comes from experiments in the SPHEX spheromak mentioned earlier. The accelerating field $E_\parallel$ has been measured and agrees with the formula in Section 5.1, and the acceleration of ions is observed directly (Rusbridge et al. 1997).

The best laboratory evidence that kink instability does not destroy jets comes from other spheromak experiments discussed below, all exhibiting a highly collimated central column despite ubiquitous kink mode activity in these experiments. Experimental evidence that the dynamos needed to produce jets do exist is being studied in experiments at the New Mexico Institute of Mining and Technology (e.g., Colgate

et al. 2011) and the University of Wisconsin–Madison (e.g., Cooper et al. 2014). Also, we note that our predicted slow propagation of magnetic jets is not inconsistent with their postulated role as a cosmic-ray accelerator. That ion acceleration along field lines to velocities $\gg dL/dt$ does not much affect jet evolution was demonstrated in experiments in the SPHEX spheromak (Rusbridge et al. 1997).

That an astrophysical jet and its return current do push away the ambient medium has been discussed and arguably confirmed in various ways. Lynden-Bell (1996, 2003) discussed this feature and assumed a return current with radius R given by balancing magnetic pressure against the ambient pressure (thermal or ram):

$$
B(R, z)^2/8\pi = p_{\mathrm{amb}}(R, z).
$$
(54)

Observationally, that the ambient medium is pushed away by radio jet/lobes is verified by the bubbles seen in galaxy clusters (McNamara & Nulsen 2007). Diehl et al. (2008) has presented analyses of radio lobes in the intracluster medium that verify Equation (54) directly. Other observational evidence that AGN jet/lobe structures create shocks by pushing aside the ambient medium has been obtained from X-ray measurements of the intracluster medium (e.g., McNamara & Nulsen 2007). Finally, the dynamics of jets punching through the ambient medium has been explored by MHD simulations in Li et al. (2006) and Nakamura et al. (2006, 2007, 2008), yielding $R(z)$ increasing slowly in z as p_{amb} decreases away from the central black hole, approximated here by a fixed large R, adequate since R appears only logarithmically in Equation (16). The simulations of Nakamura et al. (2006) also verify $B_\phi \propto 1/r$ as the dominant field component at $r > a$, as we assumed in calculating the inductance in Equation (14). Recent simulations of jets pushing into an ambient medium are also given in Carey et al. (2011), using a resistive MHD code called NIMROD with boundary conditions closely resembling those giving Figure 1 (though the nose was not blunt but somewhat pointed, probably due to a falloff of v_A with radius in these nonrelativistic simulations).

In the laboratory, jet propagation experiments have yielded direct information about how jets become collimated. Collimation near $r = 0$ is evident in Figure 2 showing simulations calibrated to measurements in the SSPX spheromak (Hooper et al. 2012), corroborated by photographic studies of the early stages of jet formation in SSPX (Romero-Talams et al. 2006). While for accretion disks we found that field lines emerge nearly vertically, the gun used in these experiments has an annular shape, causing some delay before field lines converge and straighten to form the equivalent of the central column in Figure 1. Figure 2 shows the formation of a plasma originating in an annular (coaxial) region between an inner electrode and outer electrode (the flux conserver), ejecting from the coaxial region, and forming a plasma column along the geometric axis of the flux conserver. Experimental measurements in SSPX and MHD simulations using the NIMROD code are in good agreement (Cohen et al. 2009). Figure 2 is a simulation extending in time a NIMROD run representative of SSPX in a flux conserver that is longer than that in SSPX, in order to demonstrate how astrophysical jets confined radially by Equation (54) ought to propagate away from the disk. In SSPX, the initial poloidal magnetic flux is prescribed, determined by the gun injector.

Figure 2 confirms the following interpretation of the injection of poloidal flux from the SSPX injector into a fixed flux-conserver volume. An electrical discharge forms between the electrodes, with most of the current flowing in a thin layer at the front of the plasma bubble. The resulting $\boldsymbol{j} \times \boldsymbol{B}$ force ejects the plasma, forming a bubble bounded by the return current. From the outset, the return-current channel has the characteristic blunt-nosed shape of Figure 1, confined radially by the flux conserver (Figure 2). The inner current layer pinches down to the geometric axis as the bubble expands axially, forming a current-carrying column like the central column of Figure 1. We have also verified that Corsica GS solutions converge to a pinch, even if we artificially add a large B_r at the disk, giving nonvertical flux ejection. Unlike jets formed by accretion disks, in the experiment the short length of the flux conserver is such that the plasma becomes confined in z, with time for kink modes to grow to nonlinear levels that generate reconnection events which convert the injected toroidal flux into poloidal flux, forming a spheromak, as in the closed flux of Figure 1. Until reconnection occurs, there is only a weak poloidal magnetic field inside the flux bubble; the toroidal field is formed by the current flow along the small-radius central column, dropping approximately as $1/r$ inside the bubble, as in Equation (6).

Experiments that more nearly resemble accretion-disk geometry were carried out by Bellan and coworkers (Hsu & Bellan 2003; Bellan et al. 2005), in which a small gun on axis injects helicity into a long flux conserver, though not consistently in the fast Alfvén regime, giving the behavior in Figure 2. In the laboratory experiments, even though the injector radius is smaller than the flux conserver, a small radius column forms as predicted by our model, now confirmed in MHD simulations (Zhai et al. 2014).

8. SUMMARY AND COMPARISON WITH PREVIOUS MODELS

In this paper, we have extended the calculation of magnetic fields at the surface of accretion disks in Paper I to include jet/lobes ejected from the disk when dynamo currents rise to a level sufficient to stretch magnetic field lines embedded in the disk to enormous distances. We have shown in Section 5 why jets projecting forward the field profiles produced by the disk are relatively stable over long distances, yielding in Section 6 calculations of jet dimensions in reasonable agreement with observations. In future papers, we will show how jets and especially the nose end of jets become DC particle accelerators producing UHECRs in the nose.

Like many other models in the literature, we approximate jet evolution as a sequence of quasi-static equilibrium solutions of the GS equation, with a length L growing as $dL/dt \approx 0.01$ c in Equation (18). Unlike GS models dominated by hydrodynamic "winds," much studied in the literature (e.g., Beskin 2010), we found that disk dynamics prevents the creation of winds in the large diffuse pinch zone of our solution, in Figure 1, giving GS solutions dominated instead by the coronal field of the disk as a boundary condition, joined to an electric circuit model of the central column zone where most of the current flows. The slow evolution of the jet length $L(t)$ shows that ions accelerated to relativistic velocities flow rapidly along field lines of a magnetic structure that is slowly changing. In this sense, observations attributable to relativistic ion and electron acceleration or transient superluminal wave propagation do

not imply that the magnetic jet itself is "relativistic," an essential point in comparing our studies of jet stability with analytical stability studies of relativistic jets, as discussed in Section 2.

Our new results concern our unique magnetic boundary condition for the diffuse pinch region and its influence on jet stability. In Section 3.1, we noted that the boundary condition serves to imprint the field of the disk onto the advancing jet. In the diffuse pinch zone of the disk, we find $B_\phi \approx (2I)/(cr)$ at the disk surface for current I in the central column of Figure 1, while the poloidal profile $B_z(r)$ is just that required to eject disk angular momentum as it arrives at each flux surface. For zero viscosity, all of the angular momentum is ejected magnetically, giving uniquely $B_z = (\dot{M}\Omega)/(rB_\phi) \propto r^{-3/2}$ in Equation (6). It is the falloff of B_z faster than B_ϕ that was shown to stabilize the diffuse pinch against internal modes, in Section 4. A finite viscosity dissipating some of the angular momentum inside the disk only makes B_z fall faster, as is shown in Paper I.

A boundary condition different from ours is obtained from the description of jet ejection as the winding of a magnetic flux with footprints frozen in a highly conducting disk (Li et al. 2001; Frank et al. 2002, and references therein). This was the idea behind the growing magnetic tower model (Lynden-Bell 1996, 2003). Li et al. (2001) applied flux winding as a precise boundary condition for a quasi-static GS solution of a jet embedded in an ambient environment, giving $N \approx \Delta\Omega t$ as the number of twists on a field line and $L(r) \approx r\Omega t \propto (a/r)^{1/2}$ as the vertical height of field lines across a disk with Keplerian rotation. This is distinctly different from our model, in which it is the dominant central column current that determines the nose boundary, giving a blunt-shaped nose with $L(r)$ independent of r. As discussed in Paper I, that the flux winding concept is incorrect concerns the nonideal nature of the accretion disk, allowing the return current j_r flowing radially across flux surfaces within the disk to adjust so as to conserve and recycle angular momentum in the accretion disk. The distribution of j_z exiting the disk is the determining feature, giving current concentrated in the central column where most of the gravitational energy is deposited. It is this concentration of current by gravity that yields a vacuum-like $B_\phi = (2I)/(cr)$ as the dominant field component at the disk and throughout the jet.

A feature of our accretion disk+jet model is the failure of our exact diffuse pinch disk solution at $r < a = 10R_s$, leading us to represent the central column at $r < a$ using a zero-dimensional electric circuit model. In Appendix B, we justify the circuit model by physical evidence of magnetic fields near black holes and plausible models extending our diffuse pinch solution inside the central column. Our results can be compared with Appl & Camenzind (1993), who also solve Equation (1) with finite E_r but with an assumed family of profiles, giving $I(r) = rB_\phi \to \Psi \propto r^2$ at small r. For an early analytical treatment, see models based on Blandford & Znajek (1977) and reviewed in Beskin (2010).

We conclude with a comparison of our model with general relativistic (GRMHD) simulations intended to be the definitive coupling of accretion disk dynamics to jet propagation (see, e.g., deVelliers et al. 2003; McKinney & Gammie 2004; Tchekhovskoy et al. 2008; McKinney et al. 2012). These simulations include the black hole region essential to determining the uncertain parameter b in our model, discussed further in Appendix B. Similar to our model, GRMHD

simulations usually start from a poloidal magnetic seed field with closed flux surfaces. While both approaches find that a dynamo current causes poloidal flux surfaces to expand vertically and radially, GRMHD simulations to date produce relativistic jet currents that fail to enclose the poloidal flux O point as would be necessary to produce the self-excited dynamo of our model. In Appendix C we speculate why including ambient pressure in GRMHD simulations together with the expansion of poloidal flux might eventually yield a self-excited dynamo producing the nonrelativistic jets of our model.

A more profound question may be whether GRMHD simulations can produce a sustained dynamo. While it is known that self-excited fluctuations do drive accretion in GRMHD simulations, Pariev & Colgate (2007) postulate that self-excited turbulence cannot long sustain the coherent magnetic field required to produce sustained jets. Adding to GRMHD codes, something else imposing the needed magnetic coherence, such as the star–disk collisions proposed in Pariev & Colgate (2007), might change the outcome. The Pariev–Colgate conjecture is supported by MHD simulations of star–disk collisions (but missing magneto-rotational instability; MRI) in Pariev et al. (2007), shown to be equivalent to a dynamo drive $cE_\phi = \alpha_{\mathrm{DYN}} B_\phi$ already found to be promising in the simulations in Christodoulou et al. (2008), which do include MRI using a 2.5D simulation.

APPENDIX A
WHY JETS DRIVEN BY ACCRETION DISKS ARE QUASI-STATIC

In Paper I, we discussed the conditions for an accretion disk to reach a quasi-steady state, as assumed throughout this paper. In Section 3, we found that jet magnetic fields could also be calculated as quasi-static GS equilibria, and jet dynamics could be described as one-dimensional with jet velocity dL/dt. The conditions for this were (1) pressure inside the central column zone of the jet must not exceed the pinch force due to the jet current and (2) the poloidal Alfvén speed inside the jet and in the shock front at the nose must satisfy $v_A \gg dL/dt = 0.01c$ by Equation (18). The absence of centrifugal ejection of jet mass in our model argues for low kinetic pressure in jets, and an example of a collimated jet in the presence of internal electric field pressure is given in Appendices B and C. Here we justify a fast Alfvén velocity.

A.1. Alfvén Velocity

The condition that the Alfvén velocity $v_A \gg dL/dt$ serves to reduce jet magnetic fields to the quasi-static solution inside a rigid boundary in Section 3. We take the criterion justifying our solution in Section 3 to be a plasma density n_i satisfying $B_{\mathrm{POL}}/(4\pi n_i m_i)^{1/2} \gg 0.01c$, where m_i is the mass of hydrogen. Using $B_{POL} = B_z$ from Equation (6), we get

$$n_i \ll B_{\mathrm{POL}}^2 / \left[4\pi m_i \gamma_{\mathrm{L}} (0.01c)^2 \right]$$
$$\approx 1.2 \times 10^{12} \left(1/\gamma_{\mathrm{L}} \right) M_8^{-1} (a/r)^2 \ \mathrm{cm}^{-3}, \qquad (55)$$

where we will find $\gamma_{\mathrm{L}} < (eV/m_i c^2) = 1.2 \times 10^{11}$ using Equation (45). In other words, if the plasma density inside the jet satisfies Equation (55), then the jet is in the fast Alfvén velocity limit.

For comparison, we now examine several characteristic densities. The disk density itself is from Paper I, with Ω from Equation (41)

$$n_{\mathrm{disk}} = \dot{M} / \left(m_i 2\pi r \left| v_r \right| H \right)$$
$$\approx 10^{10} M_8^{-1} (a/r) \left(\left| v_r \right| / r\Omega \right)^{-2} \ \mathrm{cm}^{-3}, \qquad (56)$$

where $\dot{M} = M/\tau = 7 \times 10^{25} M_8 \ \mathrm{gm \ s}^{-1}$ and $H/r = (a/r)^{1/2}$ from Paper I (Equations (14) and (A7) in that Paper with $g = 1$).

By contrast, the minimum density in the jet is that required to carry the jet current, given by

$$n_J \approx j_\phi / (ec) \approx 1.4 \times 10^{-3} M_8^{-3/2} (a/r)^{5/2} \ \mathrm{cm}^{-3}, \qquad (57)$$

where at large r, $j \approx j_\phi = (c/4\pi)(-\partial B_z/\partial r)$ with $B_z = B_a (a/r)^{3/2}$ from Equation (6). Finally, the ambient density is of order $n_{\mathrm{amb}} \approx 10^{-5} \ \mathrm{cm}^{-3}$ (e.g., Colgate & Li 2004, though highly uncertain).

Since the jet pushes away the ambient medium, the actual density inside the jet should be its value after ejection from the disk, plus possible mass loading along the jet due to inward transport from the ambient. We will discuss both mass supplies to the jet plasma density, showing that the condition in Equation (55) is always satisfied in AGN jets.

The density injected into jets by the disk is that which can escape the gravitational attraction of the black hole. While MHD models can create current jets from purely magnetic forces stretching field lines away from the disk, the magnetic force $\boldsymbol{j} \times \boldsymbol{B}$ acts perpendicular to $\boldsymbol{B}$, whereas the plasma required to conduct this current tends to flow parallel to $\boldsymbol{B}$ in our model. Thus some nonmagnetic force is required to eject current carriers parallel to $\boldsymbol{B}$. Mere pressure is not a likely candidate, except very near the black hole. In our accretion model in Paper I, this is compounded by the fact that the coronal boundary where the jet is ejected is the boundary where disk MHD turbulence driving accretion ceases. In our model, it is pressure due to this turbulence, not ordinary thermal heating, that balances gravity and vertical magnetic pinch forces at this boundary so that the effective pressure vanishes at the jet boundary.

In the literature, there are two paradigms that do not rely on pressure for how the current carriers required by MHD could be generated. One is a thin layer of net charge called a plasma sheath, analogous to sheaths at the gun electrodes in laboratory experiments (Lovelace 1976). The other is kinetic "winds" ejected from the disk, the model most cited being kinetic ejection by centrifugal forces along field lines sufficiently tilted away from vertical (Blandford & Payne 1982). However, in Paper I, we showed that, in a quasi-steady state, jet magnetic

fields emerge almost vertically, producing negligible centrifugal force. In Paper I, this was shown to follow from the z component of Ohm's Law, giving $B_r = (v_r/r\Omega)B_\phi \ll B_\phi, v_r$ being the accretion velocity that we expect to be much less than the rotation velocity $r\Omega$. If both pressure and centrifugal forces are negligible, we are left with electrostatic sheaths as the likely mechanism to eject current carriers as jets settle into a quasi-steady state. This is credible because the enormous voltage of the dynamo available to create a sheath greatly exceeds the gravitational binding energy (Lovelace 1976).

Current ejection by an electrostatic sheath yields the low jet density in Equation (57), unless mass loading builds up the density beyond the sheath, which is not likely, as we show in Section A.3. For this density and the field amplitude given by Equation (43), the Alfvén speed is of order $10^{16}/\gamma^{1/2} > c$, even for the largest possible $\gamma \leqslant (eV/m_i c^2)$ due to acceleration by the voltage V in Equation (45).

A.2. Electrostatic Sheaths in a Gravitational Field

An electrostatic sheath is a discontinuity in the electric field that arises to maintain current flow, not required in MHD theory. The appearance of a sheath can be derived as follows. Let B_ϕ be positive so that the region nearest the black hole serves as an anode; the opposite polarity would yield a cathode on outgoing field lines with the corresponding anode located either at the footprint where field lines return to the disk, or more probably as a virtual anode somewhere in the nose. Plasma tends to flow parallel to B. Taking s along B, we add an electrostatic field $-\partial\Phi/\partial s$ to the quasi-static axial force balance to obtain

$$m_i\big(j_{si}/ev_{si}\big)\partial v_{zi}/\partial t = \big(-nm_i\partial V_G/\partial s\big) - ne\partial\Phi/\partial s, \quad (58)$$

with gravitational potential V_G. Here $j_{si} = env_{si}$. At an anode, this is the ion contribution to the current at speed v_{si} along the twisted field lines in Figure 1, in constant ratio to v_{zi} in a straight column, giving $j_{si} \propto j_{zi}$, which is constant without mass loading. The $\partial\Phi/\partial s$ term is the only way to accelerate ions so as to maintain constant j_{si} as n falls off near the edge of the disk. As $-\partial\Phi/\partial s$ increases to do this, electrons are repelled, yielding a net charge due to ions that create the electrostatic sheath (or sometimes, a double sheath) as the condition to maintain the current.

We can approximate an anode sheath at a location $z = d$ as a Child–Langmuir sheath (Goldston & Rutherford 1995), modified to account for gravity. The modified Poisson's equation has the following form (Fowler et al. 2009a):

$$-\partial^2\Phi/\partial s^2 = \partial^2\phi/\partial s^2 - 2V_G(d)\big(d/z^3\big)$$
$$= 4\pi (I/A)\big[v_{si}^{-1} - v_{si}(Z)^{-1}\big], \quad (59)$$

$$\phi = \big(V_s - \Phi\big) - e^{-1}V_G(d)(1 - d/z), \quad (60)$$

$$v_{si} = c\left[\big(E_i^2 - m_i^2 c^4\big)^{1/2}\big/E_i\right], \quad E_i = e\phi + m_i c^2, \quad (61)$$

where $v_{si}(Z)$ is the ion velocity at $Z \gg d$ beyond the sheath, V_S is the sheath voltage, and $n_i = I/(eAv_{si})$ is the ion charge density for sheath area $A = \pi a^2$. Boundary conditions are $\phi = 0$ at $z = d$ and $\partial\phi/\partial s \to 0$ at $z = Z$. Near $z = d$, $v_{si} \ll c$, while $v_{si}(Z)$ can be of order c to ensure ion escape from gravity. Because of the abrupt change in ϕ through a sheath giving a very large electric force, in Equation (59) we can neglect the gravitational force term containing $V_G(d)$, giving a Child–Langmuir solution for ϕ with the "Debye" sheath thickness calculated as if the temperature were eV_S (Goldston & Rutherford 1995). Relativistic ions included in Equation (61) could broaden the sheath near the black hole. Exactly where the sheath forms depends on how the density drops in the disk corona.

A.3. Mass Loading beyond the Sheath

The jet nose with magnetic field equal to that of the dynamo easily pushes aside the ambient pressure at small r and continues to do so as the jet lengthens, as discussed in Section 7. This is true from the outset, the field magnitude nearest the black hole being larger with smaller mass, $B \propto M^{-1/2}$ from Equation (43). Thus, as accretion proceeds, any mass not captured within the disk remains part of the ambient medium that is pushed away. Then the jet plasma density is either that in Equation (57) or this density augmented by mass loading along the jet.

To calculate mass loading, let S be the source of mass loading given by

$$S = nn_0(\sigma v)_i + n_{amb}D/X^2, \quad (62)$$

where $(\sigma v)_i$ is the ionization rate, n_0 represents neutral atoms somehow penetrating through the return current and the diffuse pinch in Figure 1 to reach the central column, and D represents diffusion of ambient plasma from a distance X. The density along the column would be, for $v_{iz} \approx c$

$$n = \big[Sz + \big(j_{zi}/e\big)\big]\big/c = Sz\big/c + n_I, \quad (63)$$

where j_{zi} is the ion current entering the sheath, giving $n_I = n_J(a)$.

That n/n_I is in fact likely to be at most of order unity can be seen as follows. The most probable source of neutral particles would be the ionized ambient $n_{amb} \approx 10^{-5}$ cm^{-3}. Let the neutral fraction be f_I (say, an upper limit of 1%). For $(\sigma v)_i < 10^{-8}$ (>KeV electrons) and an initial $n = n_I$, $(Sz/cn_I) \ll 1$ as long as $f_I < 30\%$, which is surely true. The other likely source is stars penetrating the structure. However, stars tend to accrete mass, not deposit it, and in any case the average n_0 due to stars, of order $n_0 = (10^5/\text{pc}^3) \approx 10^{-50}$ cm^{-3} (Pariev & Colgate 2007), is much less than our upper-limit estimate for ambient neutrals and hence irrelevant.

Concerning plasma diffusion, the largest diffusion coefficient due to a random walk of Larmor orbits at the ion cyclotron frequency could give $D \approx r_L^2\omega_c \approx cE_i/(eB)$ (where E_i is the ion energy), similar to "Bohm diffusion" but with the ion energy rather than electron temperature. For kiloelectron-volt ambient ions and B_a in Equation (43), $D = 6 \times 10^7(B_a/B)M_8^{1/2}$, giving for diffusion from a distance X scaled to $a = 3 \times 10^{14}M_8$ cm and $L = 10^{24}$ cm

$$\big(Sz/cn_I\big)_{\text{DIFF}} < 10^{-10}\big(B_a/B\big)(a/X)^2(z/L) \ll 1. \quad (64)$$

The inequality holds both for radial diffusion from the return-current boundary at $X = R$ (even though $(aB_a/BR) = 1$ there) and for diffusion from the nose with $B = B_a$ and $X \gg a$ to be of interest.

APPENDIX B
CENTRAL COLUMN MAGNETIC STRUCTURE; THE PARAMETER b

Our model, developed in Paper I and reviewed in the Introduction and Sections 3.1 and 3.2 with the parameters in Section 6, is fully determined except for the voltage enhancement factor b, if we can assure ourselves that solutions to Equation (1) exist inside the jet central column. Then the associated electric field at the midplane ($z = 0$) determines b, given by

$$b = 1 + \int_{R_*}^{a} dr E_r / E_a, \qquad (65a)$$

$$E_r = c^{-1}\left[\left(r\Omega + |v_r|\right)|B_z|\right], \quad z = 0. \qquad (65b)$$

In Equation (65b), E_r comes from Equation (10) with $D_r \approx -D_\phi \approx c^{-1}|v_r||B_z|$ due to disk fluctuations, as discussed in Section 3.1. In Equation (65a), E_a is obtained by applying Equation (65b) at $r > a$ where $|v_r|$ is small, giving $E_a = (a\Omega_a/c)B_a = (1/2\sqrt{b})B_a$ by Equation (43), for $f = 1/4$.

Substituting Equation (65b) into Equation (1) with Equation (5) as a constraint allows us to extend our collimated jet solution to R_* near the black hole. The exact result depends on the unknown v_r in E_r that could be determined by the GRMHD codes discussed in Appendix C. Collimated relativistic solutions for a range of E_r profiles are given in Appl & Camenzind (1993). A similar exact cylindrical solution of the Maxwell–Einstein equations appears in Chapline & Barbieri (2014), giving our Equation (1) for zero spin of the black hole. In addition, recent interpretations of jet observations support the idea that the radio-loud AGNs of interest here must produce jets with magnetic fields very close to the black hole (Zamaninasab et al. 2014), suggesting that R_* in Equation (65a) could extend very near an event horizon due to a black hole.

Example solutions such as those in Appl & Camenzind (1993) yield a reduction in the pinch force in Equation (1) accompanied by a flattening of the B_z profile, as we assumed in calculating fields in Figure 1. In joining such solutions onto the diffuse pinch, the diffuse pinch is seen to act as a "jacket" confining and collimating the central column. Then roughly we can take B_z and B_ϕ constant in Equation (5), whereby $\Omega(r) \propto I(r) \propto r$, giving zero rotation near the black hole. Given $\Omega \to 0$, integrating Equation (5) over r shows that all or most of the angular momentum accreted from a distant region is ejected as a Poynting jet, so the near neighborhood of the black hole would serve only as a gravitational attractor in a quasi-steady state. This assumes that, though in principle a black hole with an initial spin can itself serve as a Faraday disk, the timescales are such that a black hole created by accretion has come into a quasi-steady state with the accretion disk and jet that constitute its environment. The black hole simply acquires charge and current as needed to exclude the plasma E and B.

Extended to the corona, constant $E_r \approx B_a$ at $r < a$ gives, with $B_z = B_a/[A + (r/a)^{3/2}], b \approx [1 + (v/c)(1/A)]^2 \approx 5$ (the value used in Section 3.3) for $v/c \approx A = 1/2$. A different estimate can be obtained from the analysis of Zamaninasab et al. (2014), whereby data from 76 radio-loud AGN jets give as the magnetic flux near the black hole $\Phi_{BH} \approx 50[\dot{M}c(R_s/2)^2]$. Using Equations (42) and (43), our model gives, for $f = 1/4$ and $|B_z|$ above with $A = 1/2$,

$$\Phi_{BH} \approx 2\pi \int_{R_*}^{a} rdr\, |B_z| \approx 10b^{3/4}[\dot{M}c(R_s/2)^2]. \qquad \text{Equating}$$

$10b^{3/4} \approx 50$ gives $b \approx 8$. Thus, our value $b = 5$ assumed in Section 6 appears to be reasonable, noting also that $V \propto b^{1/4}$.

APPENDIX C
GRMHD SIMULATIONS

GRMHD simulations solve Maxwell's equations together with general relativistic momentum equations that we write as

$$\text{kinetic terms} = c^{-1}j \times B + \sigma E, \qquad (66)$$

where $\sigma = \nabla \cdot E/4\pi$. For jet densities in Appendix A.1, it gives an Alfvén velocity $\approx c$. We can drop the kinetic terms representing both pressure and inertia, giving the force-free degenerate electrodynamics (FFDE) force balance equation (Meier 2012):

$$c^{-1}j \times B + \sigma E = 0. \qquad (67)$$

Our model presented in this paper drops the electric field, justified after the fact because $E/B \approx v/c$ is small except very near the black hole. Then the fact that approximately $j \times B = 0$ requires j to be parallel to B. Hence, in our model, disks can only eject current as large loops enclosing the O point, giving $B_\phi \approx (2I/cr)$ as in Equation (6), and from this a huge inductance giving $dL/dt \ll c$ in Section 3.3.

By contrast, it is found in GRMHD simulations that an Alfvén velocity $\approx c$ allows current loops that avoid the O point by folding back along the outer boundary of the outgoing jet, like a coaxial cable with negligible inductance, giving $dL/dt \approx c$. How this happens can be understood from the following example, using Faraday's Law and a current density j given by the FFDE force balance. Specifically, we have

$$\partial B_\phi/\partial t = -c\partial E_r/\partial z \;\; \to \;\; dL/dt = c\left(E_r/B_\phi\right), \qquad (68a)$$

$$j = \sigma c\left(E \times B/B^2\right) + j_\parallel \equiv j_\perp + j_\parallel. \qquad (68b)$$

In the absence of a poloidal field, Equation (68a) can give a jet at speed c if the rest mass Alfvén velocity would exceed c so that FFDE remains valid. Speed c propagation occurs if $E_r = B_\phi$, yielding $j_\parallel = 0$ and $j_\perp = \sigma c$ if $B_z = 0$. GRMHD simulations launch similar jets into a preexisting poloidal field, again giving $j_z = \sigma c$ that reverses sign (because σ does) immediately outside the central column, giving the low-inductance coaxial structure mentioned above. (In our model, σ also changes sign but not j_z coming from the return of $j_\parallel$ through the disk: see Paper I.)

That GRMHD currents should ultimately produce $dL/dt \ll c$ characterizing our model can be seen by repeating the derivation of dL/dt in Section 4, giving

$$\frac{d}{dt}\int L2\pi rdr\frac{B^2 + E^2}{8\pi} \approx \frac{dL}{dt}\left[\int_0^a 2\pi rdr\frac{B^2}{8\pi} + \int_a^R 2\pi rdr\frac{B_\phi^2}{8\pi}\right]$$

$$\approx \left(\frac{I^2}{c^2}\right)\left(\frac{dL}{dt}\right)\left[1 + \left(1 - \frac{I_\perp}{I}\right)^2 \ln\left(\frac{R}{a}\right)\right]$$

$$\approx f_{\text{dis}}\, IV \qquad (69a)$$

$$I_\perp \big/ I \approx \left\langle \pi a^2 \sigma c\left(E_r/B_\phi\right)/I \right\rangle \approx \left\langle \left(E_r/B_\phi\right)^2 \right\rangle. \qquad (69b)$$

In Equation (69a), on the second line f_{dis} represents dissipation of magnetic energy, discussed below; the unity term represents integration over the central column and its near neighborhood where any $j_\perp$ exists in GRMHD simulations, while the terms in {...} represent the region at $r > a$ where $B_\phi \approx 2(I - I_\perp)/cr$ dominates, where $I_\perp$ comes from $\boldsymbol{j}_\perp$.

In Equation (69b), $\langle...\rangle$ indicates an average over the central column and its nearby return current for GRMHD solutions. We note that though $\boldsymbol{j}_\perp$ is perpendicular to $\boldsymbol{B}$, the speed c wave in Equation (68a), approximated as a cylinder, has $j_r = B_r = 0$ along the jet. Closure of the $\boldsymbol{j}_\perp$ current loop occurs only at the nose, through an area of order πa^2. Finally, $\sigma \propto E_r(a)$ and $I \propto B_\phi(a)$ in the nose region, giving then the approximate result on the rhs of Equation (69b). Using Equation (69b), Equation (69a) gives

$$\frac{dL}{dt}\left[1 + \left\{\left[1 - \left(\frac{E_r}{B_\phi}\right)^2\right]^2 \ln\left(\frac{R}{a}\right)\right\}\right] \approx f_{\mathrm{dis}}\left(c^2\, V/I\right)$$
$$\approx f_{\mathrm{dis}}\, c. \qquad (70)$$

Noting that (cV/I) is approximately (E_r/B_ϕ) averaged over the central column, we have made approximations here such that, for $E_r = B_\phi$ and zero dissipation ($f_{\mathrm{dis}} = 1$), the solution is $dL/dt = c$, as found in GRMHD simulations. In Section 4, we find $f_{\mathrm{dis}} = (1 - f_{\mathrm{conv}})/(1 + F_{\mathrm{shock}}) = 0.25$, which is certain to slow down the jet, in which case GRMHD simulations also show that (E_r/B_ϕ) begins to fall below unity, qualitatively consistent with Equation (68a). Guan et al. (2014) and Bromberg & Tchekhovskoy (2015) have shown that dissipation of mean-field magnetic energy by nonlinear kink modes also contributes a reduction in the jet velocity, whether or not some magnetic perturbation energy is lost by particle acceleration. By Equation (70), any $f_{\mathrm{dis}} < 1$ should begin to expose the inductive factor ($\ln R/a$) that eventually gives $dL/dt = 0.01\, c$ in Equation (18), consistent with observed lengths of jets.

We conclude that, in order to represent AGN jets, GRMHD simulations should always include some kind of magnetic dissipation to slow down the jet. Even so, E_r would continue to play a prominent role near the black hole, as discussed in Appendix B. An approximate reconciliation of our model with GRMHD could be obtained by integrating Equation (1) with $B_z \approx B_a/[1 + (r/a)^{3/2}]$ as in Appendix B, yielding

$$B_\phi^2 \approx E_r^2 + B_a^2 (r/a)^{3/2} \Big/ \left[1 + (r/a)^{7/2}\right]. \qquad (71)$$

This yields our diffuse pinch "jacketing" a GRMHD-like solution with $E_r \approx B_\phi$ inside $r < a$. In subsequent papers, we will show how kinetic processes, rather than MHD, cause $E_r \approx B_\phi$ to spread across the nose (the top of the jet where the jet current returns) so as to create an ion accelerator ejecting much of the jet power as ultrahigh-energy cosmic rays.

REFERENCES

Appl, S., & Camenzind, M. 1992, A&A, 256, 354
Appl, S., & Camenzind, M. 1993, A&A, 274, 699
Asada, K., Nakamura, M., Doi, A., Nagai, H., & Inoue, M. 2014, ApJL, 781, L2
Begelman, M. C., Blandford, R. D., & Rees, M. J. 1984, RvMP, 56, 255
Bellan, P. M., You, S., & Hsu, S. C. 2005, Ap&SS, 298, 203
Beskin, V. S. 2010, Usp. Fiz. Nauk, 180, 1241 English translation, PhyU 53, 1199

Beskin, V. S., & Nokhrina, E. E. 2006, MNRAS, 367, 375
Bisnovatyi-Kogan, G. S., & Lovelace, R. V. E. 2012, ApJ, 750, 109
Blandford, R. D., & Payne, D. G. 1982, MNRAS, 199, 883
Blandford, R. D., & Znajek, R. L. 1977, MNRAS, 179, 433
Bogovalov, S. V. 1995, AstL, 21, 565
Bogovalov, S. V., & Kelner, S. R. 2010, IJMPD, 19, 39
Boozer, A. H. 1986, JPlPh, 35, 133
Bromberg, O., & Tchekhovskoy, A. 2015, MNRAS, submitted, arXiv:1508.0272
Carey, C. S., Sovinec, C. R., & Heinz, S. 2011, Univ. Wisconsin Rep., www.cptc.wisc.edu/reports, UW-CPTC 11-8.pdf
Chapline, G., & Barbieri, J. 2014, IJMPD, 23, 1450025
Chiueh, T., Li, Z.-Y., & Begelman, M. C. 1991, ApJ, 377, 462
Christodoulou, D. M., Contopoulos, I., & Kazanas, D. 2008, ApJ, 674, 388
Cohen, B. I., Romero-Talamas, C. A., Ryutov, D. D., et al. 2009, PhPl, 16, 042501
Colgate, S. A., Fowler, T. K., Li, H., & Pino, J. 2014, ApJ, 789, 144 (Paper I)
Colgate, S. A., & Li, H. 2004, CRPhy, 5, 431
Colgate, S. A., Beckley, H., Si, J., et al. 2011, PhRvL, 106, 175003
Cooper, C. M., et al. 2014, PhPl, 21, 013505
Delzanno, G. L., Evstatiev, E. G., & Finn, J. M. 2007, PhPl, 14, 072902
Deng, W., Lin, Z., & Holod, I. 2012, NucFu, 52, 023005
deVelliers, J., Hawley, J. F., & Krolik, J. 2003, ApJ, 599, 238
Diehl, S., Li, H., , C. L., Fryer, C. L., & Raferty, D. 2008, ApJ, 687, 173
Eichler, D. 1993, ApJ, 419, 111
Fowler, T. K. 1968, Thermodynamics of Unstable Plasmas, Advances in Plasma Physics Vol. 1 (New York: Interscience)
Fowler, T. K. 2004, Lawrence Livermore National Laboratory Rep. UCRL-TR-204727
Fowler, T. K., Colgate, S. A., Li, H., Bulmer, R. H., & Pino, J. 2009a, Lawrence Livermore National Laboratory Rep. LLNL-TR-414420
Fowler, T. K., Jayakumar, R., & McLean, H. S. 2009b, J. Fusion Energy, 128, 0164
Frank, J., King, A., & Raine, D. 2002, Accretion Power in Astrophysics (3rd ed.; Cambridge: Cambridge Univ. Press)
Freidberg, J. P. 2014, Ideal MHD (Cambridge: Cambridge Univ. Press)
Furth, H. P., Rutherford, P. H., & Seldberg, H. 1973, PhFl, 16, 1054
Goldston, R. J., & Rutherford, P. H. 1995, Introduction to Plasma Physics (Philadelphia: Institute of Physics Publishing)
Grad, H. 1960, RvMP, 32, 380
Guan, X., Li, H., & Li, S. 2014, ApJ, 781, 48
Hardee, P. E. 2011, in Proc. IAU Symp. 275, Jets at All Scales, ed. G. E. All Scales, R. A. Sunyaev & T. Belloni (Cambridge: Cambridge Univ. Press), 41
Harris, E. G. 1975, Introduction to Modern Theoretical Physics (New York: Wiley) Chapter 6
Hegna, C. C., & Callen, J. D. 1994, PhPl, 1, 2308
Hooper, E. B., Pearlstein, L. D., & Bulmer, R. H. 1999, NucFu, 39, 863
Hooper, E. B., et al. 2012, PPCF, 54, 113001
Homan, D. C., Lister, M. L., Kovalev, Y. Y., et al. 2015, ApJ, 798, 134
Hsu, S. C., & Bellan, P. M. 2003, PhRvL, 90, 215002
Huang, Y. M., Zweibel, E. G., & Sovinec, C. R. 2006, PhPl, 13, 092102
Hudson, B., Wood, R. D., McLean, H. S., et al. 2008, PhPl, 15, 056112
Istomin, Ya. N., & Pariev, V. I. 1996, MNRAS, 281, 1
Kato, Y., Mineshige, S., & Shibata, K. 2004, ApJ, 605, 307
Komissarov, S. S., Barkov, M. V., Vlahakis, N., & Konigl, A. 2007, MNRAS, 380, 51
Komissarov, S. S., Vlahakis, N., Konigl, A., & Barkov, M. V. 2009, MNRAS, 394, 1182
Krolik, J. H. 1999, Active Galactic Nuclei (Princeton, NJ: Princeton Univ. Press)
Kronberg, P. P., Lovelace, R. V. E., Lapenta, G., & Colgate, S. A. 2011, ApJL, 741, L15
Li, H., Lapenta, G., Finn, J. M., Li, S., & Colgate, S. A. 2006, ApJ, 643, 92
Li, H., Lovelace, R. V. E., Finn, J. M., & Colgate, S. A. 2001, ApJ, 561, 915
Li, Z.-Y., Chiueh, T., & Begelman, M. C. 1992, ApJ, 394, 459
Lister, M. L., Cohen, M. H., Homan, D. C., et al. 2009, AJ, 138, 1874
Lister, M. L., Aller, M. F., Homan, D. C., et al. 2013, AJ, 146, 120
Lovelace, R. V. E. 1976, Natur, 262, 649
Lovelace, R. V. E., & Kronberg, P. P. 2013, MNRAS, 430, 2828
Lovelace, R. V. E., Li, H., Koldoba, A. V., Ustyugova, G. V., & Romanova, M. M. 2002, ApJ, 572, 445
Lovelace, R. V. E., Rothstein, D. M., & Bisnovatyi-Kogan, G. S. 2009, ApJ, 701, 885
Lynden-Bell, D. 1996, MNRAS, 279, 389
Lynden-Bell, D. 2003, MNRAS, 341, 1360

Lynden-Bell, D. 2006, MNRAS, 369, 1167
Lyubarsky, Y. 1999, MNRAS, 308, 1006
Lyubarsky, Y. 2009, ApJ, 698, 1570
McClenaghan, J. T. 2015, PhD thesis, UC-Irvine
McKinney, J. C., & Blandford, R. D. 2009, MNRAS, 394, L126
McKinney, J. C., & Gammie, C. F. 2004, ApJ, 611, 977
McKinney, J. C., Tchekhovskoy, A., & Blandford, R. D. 2012, MNRAS, 423, 3083
McNamara, B. R., & Nulsen, P. E. J. 2007, ARAA, 45, 117
Meier, D. L. 2012, Black Hole Astrophysics (New York: Springer Praxis)
Michel, F. C. 1969, ApJ, 158, 727
Mizuno, Y., Hardee, P., & Nishikawa, K.-I. 2007, ApJ, 662, 835
Nakamura, M., & Asada, K. 2013, ApJ, 775, 118
Nakamura, M., Li, H., & Li, S. 2006, ApJ, 652, 1059
Nakamura, M., Li, H., & Li, S. 2007, ApJ, 656, 721
Nakamura, M., Tregillis, I. L., Li, H., & Li, S. 2008, ApJ, 686, 843
Narayan, R., McKinney, J. C., & Farmer, A. J. 2007, MNRAS, 375, 548
Narayan, R., Li, J., & Tchekhovskoy, A. 2009, ApJ, 697, 1681
Newcomb, W. A. 1960, AnPhy, 10, 232
Okamoto, I. 1974, MNRAS, 167, 457
ONeill, S. M., Beckwith, K., & Begelman, M. C. 2012, MNRAS, 422, 1436
Owen, F. N., Hardee, P. E., & Cornwell, T. J. 1989, ApJ, 340, 698
Pariev, V. I., & Colgate, S. A. 2007, ApJ, 658, 114
Pariev, V. I., Colgate, S. A., & Finn, J. M. 2007, ApJ, 658, 129

Pearlstein, L. D. 2014, private communication
Perucho, M. 2012, IJMPS, 8, 241
Porth, O., & Komissarov, S. S. 2015, MNRAS, 452, 1089
Robinson, D. C. 1978, NucFu, 18, 939
Romero-Talams, C. A., Holcomb, C., Bellan, P. M., & Hill, D. N. 2006, PhPl, 13, 022502
Rosenbluth, M. N., & Rutherford, P. H. 1981, in Fusion Part 1A, ed. E. Teller (New York: Academic) Chapter 2
Rusbridge, M. S., Gee, S. J., Browning, P. K., et al. 1997, PPCF, 39, 683
Rutherford, P. H. 1973, PhFl, 16, 1903
Shafranov, V. D. 1957, Zh. Tear. Fiz., 33, 710 (1958, Sov. Phys. JETP 6, 545)
Shakura, N. I., & Sunyaev, R. A. 1973, A&A, 24, 237
Spruit, H. C. 2010, The Jet Paradigm (Berlin, Heidelberg: Springer)
Taylor, J. B. 1986, RvMP, 58, 741
Tchekhovskoy, A., McKinney, J. C., & Narayan, R. 2008, MNRAS, 388, 551
Uzdensky, D. A., & MacFadyen, A. I. 2006, ApJ, 647, 1192
Vlahakis, N., & Königl, A. 2003, ApJ, 596, 1080
Walker, R. C., Ly, C., Junor, W., & Hardee, P. J. 2008, JPhCS, 131, 012053
Wardle, J. F. C., Cawthorne, T. V., Roberts, D. H., Brown, L. F., et al. 1994, ApJ, 437, 122
Zamaninasab, M., Clausen-Brown, E., Savolainen, T., & Tchekhovskoy, A. 2014, Natur, 510, 126
Zensus, J. A., Cohen, M. H., & Unwin, S. C. 1995, ApJ, 443, 35
Zhai, X., Li, H., Bellan, P. M., & Li, S. 2014, ApJ, 791, 40